Simulating the interstellar medium of galaxies with radiative transfer, non-equilibrium thermochemistry, and dust

Rahul Kannan [ORCID],[1]⋆† Federico Marinacci [ORCID],[2] Mark Vogelsberger [ORCID],[3] Laura V. Sales [ORCID],[4] Paul Torrey [ORCID],[5] Volker Springel [ORCID][6] and Lars Hernquist[1]

[1]*Center for Astrophysics | Harvard and Smithsonian, 60 Garden Street, Cambridge, MA 02138, USA*
[2]*Department of Physics and Astronomy, University of Bologna, via Gobetti 93/2, I-40129 Bologna, Italy*
[3]*Kavli Institute for Astrophysics and Space Research, Massachusetts Institute of Technology, Cambridge, MA 02139, USA*
[4]*Department of Physics and Astronomy, University of California, Riverside, 900 University Avenue, Riverside, CA 92521, USA*
[5]*Department of Astronomy, University of Florida, 211 Bryant Space Sciences Center, Gainesville, FL 32611, USA*
[6]*Max-Planck-Institut für Astrophysik, Karl-Schwarzschild-Str. 1, D-85748 Garching, Germany*

ABSTRACT

We present a novel framework to self-consistently model the effects of radiation fields, dust physics, and molecular chemistry (H_2) in the interstellar medium (ISM) of galaxies. The model combines a state-of-the-art radiation hydrodynamics module with a H and He non-equilibrium thermochemistry module that accounts for H_2 coupled to an empirical dust formation and destruction model, all integrated into the new stellar feedback framework SMUGGLE. We test this model on high-resolution isolated Milky-Way (MW) simulations. We show that the effect of radiation feedback on galactic star formation rates is quite modest in low gas surface density galaxies like the MW. The multiphase structure of the ISM, however, is highly dependent on the strength of the interstellar radiation field. We are also able to predict the distribution of H_2, that allow us to match the molecular Kennicutt–Schmidt (KS) relation, without calibrating for it. We show that the dust distribution is a complex function of density, temperature, and ionization state of the gas. Our model is also able to match the observed dust temperature distribution in the ISM. Our state-of-the-art model is well-suited for performing next-generation cosmological galaxy formation simulations, which will be able to predict a wide range of resolved (~ 10 pc) properties of galaxies.

Key words: radiative transfer – ISM: dust, extinction – ISM: general – ISM: molecules – galaxies: ISM.

1 INTRODUCTION

The formation and evolution of galaxies is governed by a complex interplay between a variety of physical processes such as gravity, gas cooling, star formation, stellar and black hole feedback, radiation, magnetic fields, cosmic rays etc. (e.g. Benson 2010; Naab & Ostriker 2017; Vogelsberger et al. 2020a). This implies that an ab initio model for galaxy formation would require self-consistent modelling of all these mechanisms. Unfortunately, the scales at which these processes operate are so disparate that it becomes impossible to model all of them properly at the same time. For example, gas inflows into the galaxy are determined by the large scale ($\sim$ Mpc) matter distribution of the Universe (van de Voort et al. 2011), gas cooling rates depend on local gas densities, temperatures, and metallicities (Wiersma, Schaye & Smith 2009), which in turn depend on the star formation and metal entrainment processes in galactic winds. These winds are launched close to star-forming regions, on scales of less than $\sim$100 parsecs (Thornton et al. 1998). The effect of radiation fields is mainly felt around newly formed stars ($\sim$1 pc; Kannan et al. 2020) while black

hole feeding and feedback require the simulations to resolve the accretion disc around the black hole ($\sim 10^{-3}$ pc; Morgan et al. 2010).

The large dynamic range necessitates the use of analytic prescriptions that translate effects occurring below the resolution level of the simulation on to the grid scale. The accuracy of these sub-resolution models has been constantly improving. Current state-of-the-art simulations are able to capture and match a wide array of galaxy properties such as the galaxy luminosity function, colour bimodality, galaxy sizes, metallicities, etc. (e.g. Kannan et al. 2014; Vogelsberger et al. 2014; Schaye et al. 2015; Davé, Thompson & Hopkins 2016; Springel et al. 2018). They are however, unable to predict the small-scale structure ($\lesssim$1 kpc) of star-forming regions. Moreover, most of these models are tuned to reproduce the observables in simulations with relatively low resolution and, therefore, it is unclear if they are adequate to simulate galaxies in a resolved manner. In recent years, increases in computational power have made it possible to simulate galaxy formation in a more resolved manner. These models have prescriptions for low temperature gas cooling and subgrid models for stellar feedback (Hopkins et al. 2014, 2018; Smith, Sijacki & Shen 2018; Marinacci et al. 2019). The resulting simulations partially resolve giant molecular clouds, which are the sites for star formation, produce a multiphase interstellar medium (ISM) in a self-consistent manner, and reproduce resolved properties of galaxies such as local

⋆ E-mail: rahul.kannan@cfa.harvard.edu
† Einstein Fellow

group dwarfs (Wetzel et al. 2016; Smith, Sijacki & Shen 2019), globular cluster formation (Ma et al. 2020), and disc morphology and kinematics (Ma et al. 2017).

While these models have introduced more realism into galaxy formation simulations, they still miss important processes like radiation fields, dust, molecular chemistry, and cosmic rays. Radiation field can affect the properties of gas in galaxies on both large and small scales. The intense radiation from newly formed young stars photoheats the surrounding high-density gas to a temperature of about 10^4 K (Strömgren 1939), driving small scale winds that reduce the density around stars before they explode, increasing the efficiency of SN feedback (Geen et al. 2015; Rosdahl & Teyssier 2015; Kannan et al. 2020). Radiation escaping these star-forming clouds will ionize the gas and metals in the ISM and circumgalactic medium (CGM), lowering the cooling rates, in turn reducing the star formation rate in galaxies (Cantalupo 2010; Kannan et al. 2014, 2016). Far-UV radiation can knock electrons off the dust grains in the ISM, which thermalize and heat the gas (Draine 1978). Radiation pressure, both by UV and trapped IR radiation can impart momentum into the ISM, which helps drive large-scale galactic winds (Murray, Ménard & Thompson 2011). While some sub-grid models exist (Hopkins et al. 2014; Hu et al. 2017; Hopkins et al. 2018; Marinacci et al. 2019), it is unclear if they accurately capture this process in a wide variety of environments (Rosdahl & Teyssier 2015; Fujimoto et al. 2019; Kannan et al. 2020).

Dust is another important component of the ISM. Interstellar dust grains are microscopic solid particles made up from metals in the ISM. Although they account for only about 1 per cent of the total ISM mass they reprocess a large fraction of starlight, reradiating it in the infrared (see e.g. Clements et al. 1996), are responsible for heating the low-density gas in the ISM via the photoelectric effect, and act as catalysts for numerous chemical reactions, including the formation of molecular hydrogen (H_2; Gould & Salpeter 1963). It is important to understand dust abundances and obscuration in order to properly quantify star formation and stellar properties of galaxies (Cochrane et al. 2019; Vogelsberger et al. 2020b). Dust also determines the escape fraction of Lyman continuum photons from star forming clouds (Kim, Kim & Ostriker 2019) and is essential in driving outflows in highly optically thick galaxies (Davis et al. 2014). Finally, molecular hydrogen is an important cooling channel in the ISM, and the star formation rate of galaxies correlates extremely well with the H_2 content even on sub-kpc scales (Leroy et al. 2008).

While these processes have been studied individually in galaxies (e.g. Glover & Mac Low 2007; McKinnon et al. 2017; Hopkins et al. 2020), their combined impact has still not been modelled simultaneously. This paper combines a state-of-the-art radiation hydrodynamics module with a non-equilibrium thermochemistry module that accounts for H_2 coupled to explicit dust formation and destruction, all integrated into a novel stellar feedback framework, the Stars and Multiphase Gas in Galaxies (SMUGGLE) model (Marinacci et al. 2019). We test this model on an isolated MW simulation at different resolutions and radiation field properties. We show that we are able to reproduce a wide range of observables of local group galaxies. In Section 2, we outline the methods used in the paper. Section 3 gives the most important results of this work and finally, Section 4, summarizes our findings and outlines the main conclusions.

2 METHODS

The simulations presented in this work are performed with AREPO-RT (Kannan et al. 2019), a radiation hydrodynamic (RHD) extension

to the moving mesh hydrodynamic code AREPO (Springel 2010; Pakmor et al. 2016). The mesh is regularized using the scheme described in Vogelsberger et al. (2012). The gravitational forces are calculated using a hierarchical octtree algorithm (Barnes & Hut 1986). Radiation fields are simulated by casting the radiative transfer equation into a set of hyperbolic conservation laws for photon number density (N_γ) and photon flux ($\mathbf{F}_\gamma$) by taking its zeroth and first moments, respectively (Kannan et al. 2019). These equations are closed using the M1 closure relation (equation 25 of Levermore 1984). The algorithm is fully conservative and compatible with the individual time-stepping scheme of AREPO. In order to prevent extremely small time-steps, we use the reduced speed of light approximation (Gnedin & Abel 2001) with $\tilde{c} = 10^3$ km s^{-1}. Furthermore, for each hydro time-step the RT step is sub-cycled eight times according to the algorithm described in Appendix A of Kannan et al. (2019). In the following subsections, we will give a brief description of the gas cooling and thermochemistry, dust physics, star formation, radiative feedback, stellar winds, and supernova (SN) feedback prescriptions used in this work.

2.1 The thermochemical network and gas cooling

The cooling function is split into four separate terms: primordial cooling from Hydrogen and Helium (Λ_p), metal cooling (Λ_M), photoelectric heating (Λ_{PE}), and cooling due to dust–gas–radiation field (Λ_D) interactions. The total cooling (Λ_{tot}) is then given by

$$\Lambda_{tot} = \Lambda_p\left(n_j, N_\gamma^i, T\right) + \frac{Z}{Z_\odot}\Lambda_M(T, \rho, z)$$
$$+ \Lambda_{PE}\left(D, T, N_\gamma^{FUV}\right) + \Lambda_D\left(\rho, T, D, N_\gamma^{IR}\right), \quad (1)$$

where T is the temperature of the gas, Z is the metallicity, $Z_\odot$ is solar metallicity, z is the redshift, D is the dust-to-gas ratio, ρ is the density of the gas cell, n_j is the number density of all the ionic species tracked in our primordial thermochemical network ($j \in [H_2, H I, H II, He I, He II, He III]$), and N_γ^{FUV} and N_γ^{IR} are the photon number density in the infra-red (IR) and far ultraviolet (FUV) bands, respectively (see Table 1 for more details). The primordial thermochemistry network couples the RHD module to the gas via photoheating and radiation pressure.

In this work, we add a simple model for molecular Hydrogen (H_2) chemistry and cooling in addition to the atomic Hydrogen and Helium thermochemistry network described by equations (49)–(51) of Kannan et al. (2019). An additional equation describing the number density evolution of H_2 is incorporated into the chemical network:

$$\frac{dn_{H_2}}{dt} = \alpha_{H_2}^D\left(\frac{D}{D_{MW}}\right)n_H n_{H I} + \alpha_{H_2}^{GP} n_{H I} n_e$$
$$+ \alpha_{H_2}^{3B} n_{H I}^2(n_{H I} + n_{H_2}/8) - \sigma_{H_2 H I} n_{H_2} n_{H I}$$
$$- \sigma_{H_2 H_2} n_{H_2}^2 - n_{H_2}\left(S_{H_2}\Gamma_{H_2}^{LW} + \Gamma_{H_2}^+\right). \quad (2)$$

This also changes equation (52) of Kannan et al. (2019) to

$$n_H = 2n_{H_2} + n_{H I} + n_{H II}, \quad (3)$$

and all other relevant equations remain the same.

In equation (2), $\alpha_{H_2}^D$ is the formation rate of molecular hydrogen on dust grains, D is the dust-to-gas ratio (modelled self-consistently using the dust model described in Section 2.2), D_{MW} is the dust-to-gas ratio in the Milky-Way (MW; 0.01), $\alpha_{H_2}^{GP}$ is the formation rate of molecular hydrogen in the gas phase, $\alpha_{H_2}^{3B}$ is the formation rate through three-body interactions, $\sigma_{H_2 H I}$ and $\sigma_{H_2 H_2}$ are the collisional destruction rates due to collisions between H I and H_2, and H_2 and

Table 1. Table outlining the frequency discretization of the radiation field as used in our simulations. It lists the frequency bin name (first column), the frequency range it covers (second column), the mean ionization cross-section (σ, equation (20)) for the different species (H$_2$, third column; H I, fourth column; He I, fifth column; He II, sixth column), the mean photoheating rate ($\hbar$, equation 24) for the different species (H$_2$, seventh column; H I, eighth column; He I, ninth column; He II, tenth column), the mean radiation pressure (p, equation 26) for the different species (H$_2$, eleventh column; H I, twelfth column; He I, thirteenth column; He II, fourteenth column), the mean energy per photon ($\mathcal{E}$, fifteenth column), and the opacity to dust grains ($\kappa_{\rm d}$, sixteenth column). While the dust opacities for the optical, UV, and ionizing bins are constant, the IR opacities are calculated assuming a certain grain size distribution and dust temperature as outlined in Appendix C of Kannan et al. (2019).

Bin	Range (eV)	$\sigma_{\rm H_2}$ (Mb)	$\sigma_{\rm H I}$ (Mb)	$\sigma_{\rm He I}$ (Mb)	$\sigma_{\rm He II}$ (Mb)	$\hbar_{\rm H_2}$ (eV)	$\hbar_{\rm H I}$ (eV)	$\hbar_{\rm He I}$ (eV)	$\hbar_{\rm He II}$ (eV)	$p_{\rm H_2}$ (eV)	$p_{\rm H I}$ (eV)	$p_{\rm He I}$ (eV)	$p_{\rm He II}$ (eV)	$\mathcal{E}$ (eV)	$\kappa_{\rm d}$ (cm^2 g^{-1})
IR	0.1–1	0	0	0	0	0	0	0	0	0	0	0	0	0.65	f($T_{\rm d}$)
Opt	1–5.8	0	0	0	0	0	0	0	0	0	0	0	0	3.67	150
FUV	5.8–11.2	0	0	0	0	0	0	0	0	0	0	0	0	8.45	1500
LW	11.2–13.6	0.21	0	0	0	0	0	0	0	12.26	0	0	0	12.26	1000
EUV1	13.6–24.6	5.09	3.37	0	0	3.78	3.15	0	0	18.98	16.75	0	0	18.01	1000
EUV2	24.6–54.4	2.42	0.79	5.10	0	14.75	13.10	3.81	0	28.35	28.30	28.41	0	29.89	1000
EUV3	54.4–∞	0.32	0.11	0.77	1.42	41.18	42.78	31.80	2.03	56.38	56.38	56.40	56.43	56.85	1000

H$_2$ respectively, $\Gamma_{\rm H_2}^{\rm LW}$ is the photodissociation rate due to Lyman–Werner band (11.2–13.6 eV) photons, and $\Gamma_{\rm H_2}^+$ is the photoionization rate due to photons with energies greater than 15.2 eV. The value of all these coefficients are taken from Nickerson, Teyssier & Rosdahl (2018). $S_{\rm H_2}$ is the shielding factor due to molecular hydrogen (see equation A5 of Gnedin & Kravtsov 2011). We follow Draine & Bertoldi (1996) and define this factor as

$$S_{\rm H_2} = \frac{1 - \omega_{\rm H_2}}{(1 + \chi)^2} + \frac{\omega_{\rm H_2}}{\sqrt{1 + \chi}} e^{-0.00085\sqrt{1+\chi}}, \qquad (4)$$

where $\omega_{\rm H_2} = 0.2$ and $\chi = N_{\rm H_2}/(5 \times 10^{14}\,{\rm cm}^{-2})$. The column density $N_{\rm H_2}$ is obtained by using the Sobolev approximation $N_{\rm H_2} = n_{\rm H_2} L_{\rm sob}$, where $L_{\rm sob} = \rho/2|\nabla\rho|$. The self-shielding factor is necessary because our RT implementation does not capture the self-shielding due to line overlap (see Draine & Bertoldi 1996, for more details).

The cooling/heating rates for atomic Hydrogen and Helium are taken from Katz, Weinberg & Hernquist (1996) and Kannan et al. (2019). The cooling due to molecular hydrogen is given by

$$\Lambda({\rm H_2}) = \Lambda(n \to 0)_{\rm H_2 H_1} n_{\rm H_2} n_{\rm H 1} + \Lambda(n \to 0)_{\rm H_2 H_2} n_{\rm H_2}^2, \qquad (5)$$

where $\Lambda(n \to 0)_{\rm H_2 H_1}$ and $\Lambda(n \to 0)_{\rm H_2 H_2}$ are the low-density limits of the H$_2$ collisional cooling coefficients as described in Hollenbach & McKee (1979). We ignore UV pumping heating and H$_2$ formation heating as they are subdominant in the regimes we consider (Nickerson et al. 2018). Cosmic ray ionization and heating are included in a very crude manner by assuming canonical MW ionization and heating rates of (Indriolo & McCall 2012)

$$\Gamma_{\rm H_2}^{\rm cr} = 3.5 \times 10^{-16}\,{\rm s}^{-1},$$
$$\Gamma_{\rm H 1}^{\rm cr} = 1.78 \times 10^{-16}\,{\rm s}^{-1},$$
$$\Gamma_{\rm He I}^{\rm cr} = 1.1\,\Gamma_{\rm H 1}^{\rm cr} \text{ and}$$
$$\Lambda_{\rm cr} = -1.6022 \times 10^{-11}(\Gamma_j^{\rm cr}\, n_j)\,{\rm erg\ cm}^{-3}\,{\rm s}^{-1}, \qquad (6)$$

where $j \in [{\rm H_2, H 1, He I}]$.

Metal-line cooling is implemented assuming ionization equilibrium for a given portion of dust-free and optically thin gas in a UV background radiation field given by Faucher-Giguère et al. (2009). The cooling rate $\Lambda_{\rm M}$ is computed from a look-up table containing the pre-calculated cooling values computed from CLOUDY (see Vogelsberger et al. 2013, for more details).

Photoelectric heating due to far ultraviolet (FUV; 5.8–11.2 eV) photons knocking off electrons from dust grains has been shown to be an important source of heating in the interstellar medium of galaxies (see for e.g. Bialy & Sternberg 2019). This heating rate is given by (Wolfire et al. 2003):

$$\Lambda_{\rm PE} = -1.3 \times 10^{-24} \left(\frac{D}{D_{\rm MW}}\right) \epsilon_{\rm ff} G n_{\rm H}\,{\rm erg\ cm}^{-3}\,{\rm s}^{-1}, \qquad (7)$$

where 'G' is the flux if the FUV band normalized to 1.7 times the Habing value ($G_0 = 1.6 \times 10^{-3}\,{\rm erg\ s}^{-1}\,{\rm cm}^{-2}$; Habing 1968) and

$$\epsilon_{\rm ff} = \frac{4.87 \times 10^{-2}}{1 + 4 \times 10^{-3}(2\,G_0\sqrt{T}/n_e)^{0.73}} + \frac{3.65 \times 10^{-2}(T/10^4)^{0.7}}{1 + 2 \times 10^{-4}(2\,G_0\sqrt{T}/n_e)}. \qquad (8)$$

The final cooling term we implement is that due to dust–gas energy ($\Lambda_{\rm gd}$) exchange via collisions. The rate of dust–gas energy exchange is given by (Burke & Hollenbach 1983)

$$\Lambda_{\rm gd} = n_{\rm gr} n_{\rm H} \sigma_{\rm gr} \overline{\alpha_T} 2k_B \sqrt{\frac{8k_B T}{\pi m_p}} (T - T_d), \qquad (9)$$

where $n_{\rm gr}$ is the number density of dust grains, $\sigma_{\rm gr}$ is the collisional cross-section of the dust grains, T is the gas temperature, $T_{\rm d}$ is the dust temperature, and $\overline{\alpha_T}$ is the 'average accommodation coefficient'. If we assume that the dust grains have size 'a' with density $\rho_{\rm gr}$ and the hydrogen mass fraction is $X_{\rm H}$, then equation (9) can be rewritten as

$$\Lambda_{\rm gd} = \left(\frac{3\rho_{\rm d}}{4\pi\rho_{\rm gr}a^3}\right) \left(\frac{\rho_g X_{\rm H}}{m_p}\right) (\pi a^2)\overline{\alpha_T} 2k_B \sqrt{\frac{8k_B T}{\pi m_p}} (T - T_{\rm d}), \qquad (10)$$

by setting $\rho_{\rm d} = D\rho_g$, $\rho_{\rm gr} = 2.4\,{\rm g\ cm}^{-3}$, $X_{\rm H} = 0.76$, and $\overline{\alpha_T} = 0.5$ (see fig. 4 of Burke & Hollenbach 1983) and rearranging the terms we get

$$\Lambda_{gd} = \beta \left(\frac{D}{0.01}\right) \left(\frac{0.1\mu m}{a}\right) \sqrt{\frac{T}{1\,{\rm K}}} \left(\frac{T - T_d}{1\,{\rm K}}\right) \left(\frac{n_H}{1\,{\rm cm}^{-3}}\right)^2, \qquad (11)$$

where

$$\beta = \left(\frac{3\,m_p\,\overline{\alpha_T}\,2k_B}{4\rho_{\rm gr}\,X_{\rm H}}\right) \sqrt{\frac{8k_B}{\pi m_p}} \left(\frac{0.01}{0.1\mu m}\right) \left(\frac{(1\,{\rm K})^{3/2}}{(1\,{\rm cm}^3)^2}\right)$$
$$= 1.356 \times 10^{-33}\,{\rm erg\ cm}^{-3}\,{\rm s}^{-1}. \qquad (12)$$

The two unknowns in this equation are the dust-to-gas ratio (D) and the dust temperature ($T_{\rm d}$) which are self-consistently calculated

from the empirical dust model described in the next section. We note that the size of dust grains is fixed at 0.1 µm in this work. This is potentially problematic, because the dust cooling rate for a realistic size spectrum is dominated by the smallest grains and might therefore lead to an underprediction of the cooling rate. However, this assumption will not adversely affect the temperature structure of gas in our simulations, because this cooling channel becomes relevant only in extreme high-density regions, which would already be star-forming in our model.

2.2 Dust physics

In this section, we briefly describe the self-consistent dust formation and destruction model used in our simulations (see McKinnon et al. 2017, for more details). The model tracks the dust mass for five chemical species (C, O, Mg, Si, and Fe) for each gas cell. The size of the dust grains is assumed to be constant throughout the simulation ($a = 0.1$ µm). The dust is assumed to be dynamically coupled to the gas and is passively advected along with it (see McKinnon et al. 2018, for a live dust implementation). The model accounts for three distinct dust production channels namely, SNII, SN Ia, and asymptotic giant branch (AGB) stars. The dust produced during the mass return from these stars follows the prescriptions outlined in Dwek (1998).

The mass of dust in the ISM increases due to the gas-phase metals depositing on to existing grains which is modelled according to the prescription of Dwek (1998) and Hirashita (1999):

$$\frac{dM_{dust}}{dt} = \left(1 - \frac{M_{dust}}{M_{metal}}\right)\left(\frac{M_{dust}}{\tau_g}\right), \tag{13}$$

where M_{dust} and M_{metal} are the total mass of dust and metals in the cell, and τ_g is the characteristic dust growth time-scale. This time-scale depends on the density and temperature of the gas and is given by (Yozin & Bekki 2014; Zhukovska 2014):

$$\tau_g = \tau_g^{ref}\left(\frac{\rho^{ref}}{\rho}\right)\sqrt{\frac{T^{ref}}{T}}, \tag{14}$$

where τ_g^{ref} is a normalization which depends on atom–grain collision sticking efficiencies and grain cross-sections and is set to 200 Myr. ρ^{ref} and T^{ref} are the reference density and temperature set to 1 H atom cm^{-3} and 20 K, respectively.

Dust is destroyed through shocks from SN remnants (for e.g. Seab & Shull 1983) and thermal sputtering (for e.g. Draine & Salpeter 1979).

$$\frac{dM_{dust}}{dt} = -\frac{M_{dust}}{\tau_d} - \frac{3\,M_{dust}}{\tau_{sp}}, \tag{15}$$

where τ_d is the dust destruction time-scale due to SN shocks and is given by

$$\tau_d = \frac{m_{gas}}{\beta\eta M_s(100)}, \tag{16}$$

where m_{gas} is the mass of the cell, η is the local Type II SN rate, $\beta = 0.3$, is the grain destruction efficiency in SN shocks, and $M_s(100) = 6800\,M_\odot$, is the amount of gas mass accelerated to at least 100 km s^{-1} (McKee 1989). Recent results suggest that $M_s(100)$ and β will depend on the SN rate, environment, and the properties and size of the dust grains (Hu et al. 2019; Zhu et al. 2019). However, more work needs to be done in order to quantify the dependence of these parameters in a variety of environments. Therefore, we use the simple relation (which has been shown to reproduce a wide variety of dust properties; McKinnon, Torrey & Vogelsberger 2016; McKinnon et al. 2017) in

this work, with the goal to improve it once the physics is better understood.

The sputtering time-scale is given by (Tsai & Mathews 1995)

$$\tau_{sp} = (0.17\,\text{Gyr})\left(\frac{a}{0.1\mu m}\right)\left(\frac{10^{-27}\,\text{g cm}^{-3}}{\rho}\right)\left[\left(\frac{T_0}{T}\right)^\omega + 1\right], \tag{17}$$

where $T_0 = 2\times 10^6$ K is the temperature above which the sputtering rate is constant and $\omega = 2.5$ controls the fall off in the sputtering rate at low temperatures.

In this work, we additionally include a model to track the temperature of dust grains. In the previous section, we outlined the equations governing the energy exchange between gas and dust due to collisions (equation 12). The other important process of energy exchange is between the dust and the infra-red (0.1–1 eV) radiation field. This energy exchange rate is given by (Kannan et al. 2019):

$$\Lambda_{dr} = \kappa_P\,\rho\,c\,\left(aT_d^4 - E_{IR}\right), \tag{18}$$

where κ_P is the Planck mean opacity, T_d is the dust temperature, c is the speed of light, a is the radiation constant, and E_{IR} is the energy density of photons in the IR bin. κ_P is calculated based on the local dust properties of the cell as outlined in Appendix C of Kannan et al. (2019). Since dust grains reach thermal equilibrium on a rapid time-scale (Woitke 2006), we calculate the dust temperature T_d by solving the instantaneous equilibrium condition $\Lambda_{gd} + \Lambda_{dr} = 0$ using Newton's method for root-finding. Due to the strong coupling between the dust and the radiation field, the dust temperatures are set overwhelmingly by radiative equilibrium.

2.3 Star formation

Cold gas in our simulations is converted to star particles using the usual probabilistic approach outlined in Springel & Hernquist (2003). Stars are assumed to form only above a density threshold of $n_{th} = 10^3$ cm^{-3}. The star formation efficiency is a free parameter which is set to $\epsilon = 0.01$. Additionally, following the SMUGGLE implementation, we impose the condition that the star forming gas cloud needs to be self-gravitating in order to form stars (equation 9; Marinacci et al. 2019). Although we do follow the formation of molecular hydrogen in our simulations, we choose not to tie the star formation rate to the abundance of H$_2$, with the goal of recovering the molecular Kennicutt–Schmidt (Bigiel et al. 2008; Leroy et al. 2008) relation naturally in our simulations without the need to impose it.

2.4 Stellar feedback prescriptions

We implement three feedback mechanisms related to young stars, namely, radiative feedback, stellar winds from young (O, B) stars, and AGB stars and SN feedback. We retain the SN and stellar wind feedback prescriptions of SMUGGLE and replace the subgrid radiation feedback prescriptions for photoheating and radiation pressure with accurate radiation hydrodynamics. A brief description of the implementation of all three mechanisms is given below.

2.4.1 Radiative feedback

The main radiative feedback mechanisms, namely, photoheating, radiation pressure, and photoelectric heating are modelled self-consistently through the radiative transfer scheme. In our simulations, the newly formed star particles are a source of local radiation. The

luminosity and spectral energy density is a complex function of age and metallicity taken from Bruzual & Charlot (BC03; 2003). To increase the probability of resolving the Strömgren radius, we inject all the photons in the nearest two cells closest to the star particle. Additionally, the direction of the photon flux ($\mathbf{F}_\gamma$) is set to be radially outwards from the star particle and the magnitude is $|\mathbf{F}_\gamma| = \tilde{c}E_\gamma$. This ensures that the full radiation pressure force is accounted for even if the cell optical depth is larger than one. However, this leads to anisotropic pressure forces around a star particle, but this is mitigated by the fact that we form a large number of stars during the simulation and each random orientation adds up to create an isotropic pressure force (Kannan et al. 2020).

We include photoionization and photoheating of H_2, H I, He I, and He II species. The photoionization rate for each species 'j' due to the radiation bin 'i' is given by

$$\dot{n}_j = -\tilde{c}n_j\Sigma_i\overline{\sigma}_{ij}N_\gamma^i, \tag{19}$$

where $\overline{\sigma}_{ij}$ is the mean ionization cross-section of photons in bin 'i' for interacting with species 'j' and is given by

$$\bar{\sigma}_{ij} = \frac{\int_{\nu_{i1}}^{\nu_{i2}} \frac{4\pi J_\nu}{h\nu}\sigma_{j\nu}\,\mathrm{d}\nu}{\int_{\nu_{i1}}^{\nu_{i2}} \frac{4\pi J_\nu}{h\nu}\,\mathrm{d}\nu}. \tag{20}$$

In this equation

$$J_\nu = \frac{1}{4\pi}\int_{4\pi} I_\nu\,\mathrm{d}\Omega, \tag{21}$$

$\sigma_{j\nu}$ is the frequency-dependent cross-section of species 'j', and h is the Planck constant.

Similarly, the total photoheating rate is given by

$$\mathcal{H} = \sum_j n_j\Gamma_j, \tag{22}$$

where

$$\Gamma_j = \tilde{c}\sum_i N_\gamma^i\,\bar{\sigma}_{ij}\,\mathfrak{h}_{ij}. \tag{23}$$

The mean photoheating rate $\mathfrak{h}_{ij}$ is

$$\mathfrak{h}_{ij} = \frac{\int_{\nu_{i1}}^{\nu_{i2}} \frac{4\pi J_\nu}{h\nu}\sigma_{j\nu}(h\nu - h\nu_{tj})\,\mathrm{d}\nu}{\int_{\nu_{i1}}^{\nu_{i2}} \frac{4\pi J_\nu}{h\nu}\sigma_{j\nu}\,\mathrm{d}\nu}, \tag{24}$$

where ν_{tj} is the threshold frequency for the ionization of species 'j'.

The radiation pressure term is added as a source term in the momentum conservation equation of hydrodynamics and is given by

$$\frac{\partial\rho\upsilon}{\partial t} = \frac{1}{c}\sum_i \mathbf{F}_\gamma^i\left(\sum_j n_j\,\bar{\sigma}_{ij}\,p_{ij} + \kappa_i\,\rho\,e_i\right), \tag{25}$$

where

$$p_{ij} = \frac{\int_{\nu_{i1}}^{\nu_{i2}} 4\pi J_\nu\,\sigma_{j\nu}\,\mathrm{d}\nu}{\int_{\nu_{i1}}^{\nu_{i2}} \frac{4\pi J_\nu}{h\nu}\sigma_{j\nu}\,\mathrm{d}\nu}, \tag{26}$$

κ_i is the opacity due to dust, and e_i is the mean photon energy of bin 'i'. Moreover, the IR scattering scheme described in Section 3.2.2 of Kannan et al. (2019) automatically takes care of IR radiation pressure and the momentum boost at high optical depths, without the need for subgrid models.

It is clear that the mean ionization cross-section, photoheating rate, and the mean radiation pressure terms vary from cell to cell due to the differing shapes of the radiation spectrum from different age and metallicity sources. The M1 scheme is not able to track

this change in shape. We note that for the Bruzual & Charlot (2003) spectra, the calculated radiation parameters are roughly constant and do not vary significantly with the metallicity and age of the star (see figure B2 of Rosdahl et al. 2013). We therefore calculate them using the solar metallicity – 10 Myr spectrum and use the same values for all the cells throughout the simulation. We discretize the radiation field in six radiation bins, namely, the infra-red (IR, 0.1–1 eV) bin, the optical bin (Opt, 1–5.8 eV), the far ultra violet bin (Opt, 5.8–11.2 eV), the Lyman–Warner band (LW, 11.2–13.6 eV), hydrogen ionizing bin (EUV1, 13.6–24.6 eV), He I ionizing bin (EUV2, 24.6–54.4 eV), and finally the He II ionizing bin (EUV3, 54.4–∞ eV). The mean ionization cross-section, photoheating rate, and mean radiation pressure for each of the bins are tabulated in Table 1.

Finally, photoelectric heating is implemented using equation (7) described in Section 2.1. The flux of the radiation field in the FUV band is estimated in a self-consistent manner from out RT module. The frequency range of photons that instigate photoelectric heating is from 5.8 to 11.2 eV.

2.4.2 Stellar winds

Stellar winds from young massive OB ($\gtrsim 8\,\mathrm{M}_\odot$) stars and the asymptotic giant branch (AGB) stars contribute significantly to stellar feedback. We include stellar winds according to the SMUGGLE model described in Marinacci et al. (2019). Briefly, the momentum input is computed in two parts. First, the mass-loss from OB and AGB stars is calculated according to the analytic prescription given in Hopkins et al. (2018b). The mass-loss is quantified as a function of both the age of the star and its metallicity.

The energy of the stellar wind is then computed as

$$E_{\mathrm{winds}} = \delta t\,L_{\mathrm{kin}} = M_{\mathrm{loss}}\,\psi\,10^{12}\,\mathrm{erg\,g}^{-1}, \tag{27}$$

where M_{loss} is the mass-loss rate and

$$\psi = \frac{5.94\times10^4}{1 + \left(\frac{t}{2\,\mathrm{Myr}}\right)^{1.4} + \left(\frac{t}{10\,\mathrm{Myr}}\right)^5} + 4.83. \tag{28}$$

Therefore, the total momentum of the wind is

$$p_{\mathrm{winds}} = \sqrt{2\,M_{\mathrm{loss}}\,E_{\mathrm{winds}}}. \tag{29}$$

The mass, momentum, and energy from stellar winds are injected in a continuous manner in the rest frame of the star and then transformed back into the reference frame of the simulations.

2.4.3 Supernova feedback

Feedback from SN plays a crucial role in regulating star formation rate of low mass galaxies (e.g. Kannan et al. 2014). We implement a boosted momentum injection method (Hopkins et al. 2018b; Marinacci et al. 2019) that takes into account the cooling loses that occur due to the inability to resolve the Sedov–Taylor phase. The momentum input per SN event into a neighbouring cell 'i' is

$$\Delta p_i = \tilde{w}_i\,\min\left[p_{\mathrm{SN}}\sqrt{1 + \frac{m_i}{\Delta m_i}},\,p_t\right], \tag{30}$$

where $p_{\mathrm{SN}} = \sqrt{2M_{\mathrm{SN}}E_{\mathrm{SN}}}$ is the SN momentum carried by the SN event at the time of explosion, $\tilde{w}_i$ is a weight function dividing the energy and momentum injection, m_i is the mass of the gas cell, Δm_i is the mass released during the SN event, and p_{t} is the terminal momentum, which is defined as the momentum of the SN blast

Table 2. The parameters of the Milky-Way like disc used as the initial condition for the simulations.

Galaxy	$M_{\rm halo}$ (M$_\odot$)	v_{200} (km s^{-1})	c	$M_{\rm bulge}$ (M$_\odot$)	a (kpc)	$M_{\rm disc}$ (M$_\odot$)	$r_{\rm d}$ (kpc)	h (pc)	$M_{\rm gas}$ (M$_\odot$)	$r_{\rm g}$ (kpc)	$f_{\rm gas}$ ($R < R_\odot$)	$L_{\rm box}$ (kpc)
MW	1.53×10^{12}	169	12	1.5×10^{10}	1.0	4.74×10^{10}	3.0	300	9×10^9	6.0	0.1	857

Table 3. Table of the simulations reported in this work and simulation parameters such as the model name (first column), mass of stars in the disc (second column), mass of stars in the bulge (third column), maximum mass of newly formed stellar particles (fourth column), minimum mass of gas particles (fifth column), softening length of stars (sixth column) and stars (seventh column), and the model description (eighth column).

Simulation	$m_{\star, \rm disc}$ (M$_\odot$)	$m_{\star, \rm bulge}$ (M$_\odot$)	$m_{\star, \rm max}$ (M$_\odot$)	$m_{\rm gas}$ (M$_\odot$)	$\epsilon_\star$ (pc)	$\epsilon_{\rm gas}$ (pc)	Model
MW-high	1.9×10^3	2.3×10^3	2.8×10^3	1.4×10^3	7.1	3.6	Fiducial
MW-low	1.5×10^4	2×10^4	2.2×10^4	1.1×10^4	21.4	10.7	Fiducial
MW-low-no-old	1.5×10^4	2×10^4	2.2×10^4	1.1×10^4	21.4	10.7	No old stars
MW-low-no-RT	1.5×10^4	2×10^4	2.2×10^4	1.1×10^4	21.4	10.7	No radiation fields

when it transitions from the Sedov–Taylor phase to a momentum-conserving phase

$$p_t = 4.8 \times 10^5 \, E_{\rm SN,tot}^{13/14} \left(\frac{\langle n_{\rm H} \rangle}{1 \, {\rm cm}^{-3}} \right)^{-1/7} \left(\frac{\langle Z \rangle}{Z_\odot} \right)^{-0.21} \, {\rm M}_\odot \, {\rm km \, s}^{-1}. \tag{31}$$

Here, $\langle n_{\rm H} \rangle$ and $\langle Z \rangle$ are the average density and metallicity of the gas surrounding the star particle which has undergone the SN event. Moreover, since SN explosions are discrete events, the model mimics their discrete nature by imposing a time-step constraint for each stellar particle based on its age, such that the expectation value for the number of SN events per time-step is of the order of unity. This form of SN feedback has been shown to regulate the star formation rate in low mass galaxies in a variety of environments (Hopkins et al. 2018b; Marinacci et al. 2019).

2.5 Initial conditions

We study the role of radiation fields, molecular chemistry, and dust physics in an isolated galaxy environment of a Milky-Way (MW) type galaxy (as in Marinacci et al. 2019). We construct the initial conditions following the techniques described in Hernquist (1993) and Springel, Di Matteo & Hernquist (2005). The initial galaxy is setup with a dark matter halo, a bulge, and stellar and gaseous discs. The DM halo and the bulge are modelled with a Hernquist profile (Hernquist 1990) with a scale length a. The gas and the stellar disc have an exponential profile in the radial direction with an effective radius $r_{\rm g}$ and $r_{\rm d}$, respectively. The vertical profile of the stellar disc follows a sech^2 functional form with the scale height h. The vertical profile of the gaseous disc is computed assuming hydrostatic equilibrium, with the initial gas temperature set to 10^4 K. The gas in the disc has a metallicity equal $Z = Z_\odot = 0.0127$ (Asplund et al. 2009). The lack of cosmological gas inflow on to the disc can generate unrealistic gas metallicities. To avoid this, the material returned from stars to the ISM has the same chemical composition of the star particle (i.e. production of new heavy elements is turned off). In this way the initial metallicity does not increase with time. Dust enrichment from SNe and AGB stars is, however, still active. This creates a slight inconsistency in the metal and dust enrichment models. However, this discrepancy is relatively small because almost all the dust in our simulations arises from metal deposition on to existing dust grains. The amount of dust produced by just SNe and AGB stars

is much smaller in comparison, in agreement with previous works (McKinnon et al. 2016). So we are fairly certain that we get the correct dust-to-gas ratios. On the other hand, fully cosmological simulations (which will be the subject of a forthcoming paper) are needed to gain insights into the dust-to-metal ratios in galaxies. Finally, the dark matter halo is modelled as a static background gravitational field, that is not impacted by the baryonic physics. All our simulations are evolved for $\sim$1 Gyr using the scheme described in Section 2. The structural parameters of the galaxies under consideration are given in Table 2.

The galaxy setup is run at two different resolutions termed 'low' and 'high'. We run three low resolution runs, one containing the fiducial model, another the fiducial model without contribution to the radiation from old stars, defined as stars already present initially (we assign an age of 5 Gyr to all these stars), and finally the fiducial runs minus any local radiation fields. The single high resolution run employs the fiducial model. This set of simulations is used to understand the contribution of different radiation fields and also to test the convergence of our model. The simulations we perform and the respective parameters are tabulated in Table 3.

3 RESULTS

We start with a visual inspection of the simulated galaxy. Fig. 1 shows the face-on false colour Red–Yellow–Blue (RYB) image (bottom panel) of the disc in the MW-high run after 1 Gyr of evolution. The RYB image is constructed from the IR (top left-hand panel), optical (top middle panel), and the extreme UV (EUV1, top right-hand panel) radiation fields that are self-consistently generated in the simulation. The dust lanes are clearly visible in the optical image. Moreover, the IR and Optical images show spatial anticorrelation because dust absorbs the optical light and re-emits it in IR. The EUV1 map shows a clustered appearance with the high energy radiation escaping through the low density channels that have been cleared out by early stellar radiative and SN feedback mechanisms. Moreover, we can clearly identify both obscured and unobscured star formation by focusing on the peaks of the IR and EUV1 maps, respectively.

Fig. 2 shows the star formation rate history as a function of simulation time for the 'MW-high' (red curve), 'MW-low' (blue curve), 'MW-low-no-old' (orange curve), and 'MW-low-no-RT' (green curve) runs. The star formation rate rises steeply in all cases within the first 10 Myr as the disc settles. This initial starburst is
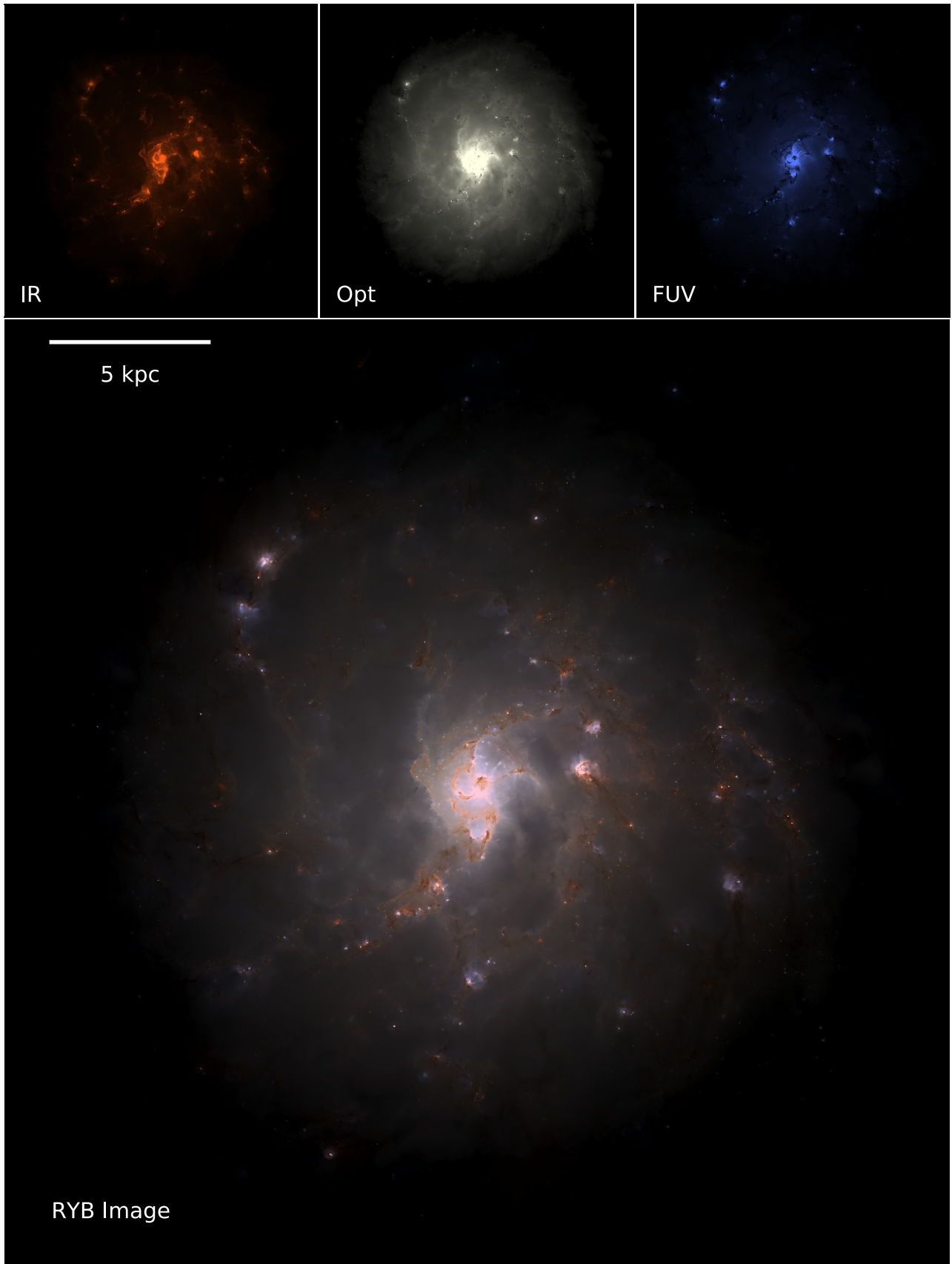
Figure 1. IR (top left-hand panel), Optical (top centre), Far-UV (top right-hand panel), and false colour RYB composite image (bottom panel) of the MW-high run after 1 Gyr of evolution.
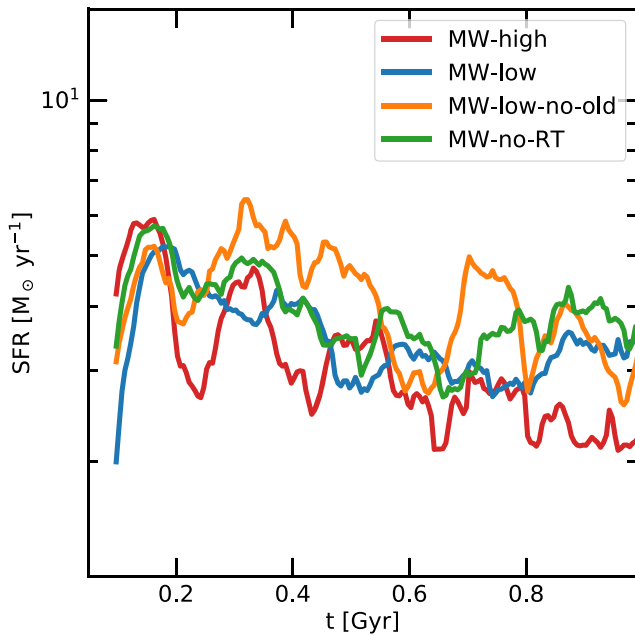
Figure 2. The star formation rate history as a function of simulation time for the 'MW-high' (red curve), 'MW-low' (blue curve), 'MW-low-no-old' (orange curve), and 'MW-low-no-RT' (green curve) runs.

prevalent across all models and reaches a value of about $\sim 6\,M_\odot\,\mathrm{yr}^{-1}$. The star formation then subsides and maintains a constant value of about 2–$4\,M_\odot\,\mathrm{yr}^{-1}$. In these low gas surface density environments, the effect of radiation feedback on kpc-averaged galactic star formation rates is modest. This is in agreement with previous studies, which have come to the same conclusion (Rosdahl & Teyssier 2015; Hopkins et al. 2020; Kannan et al. 2020). We note that the star formation rates are well converged with resolution with the MW-high simulation showing only a slight decrease in star formation compared to the corresponding low resolution run.

3.1 Impact of radiation fields on the structure of the ISM

We now concentrate on the impact of radiation fields on the multiphase structure of the ISM. To do this, we compare the MW-high and the MW-low-no-RT simulations. We note that the ISM structure in the MW-low and MW-low-no-old runs are similar to the MW-high run. Accordingly, Fig. 3 shows a 2D mass histogram of the gas in the temperature–density plane of the MW-high (left-hand panel) and MW-low-no-RT (right-hand panel) simulations. The low density gas in neither run is able to cool below $\sim 10^4$ K, due to heating from the ultraviolet background (UVB). Only the gas above the self-shielding density threshold of $n \sim 10^{-2}\,\mathrm{cm}^{-3}$ manages to cool below this temperature. The phase-space structure of gas above this density is markedly different in the two runs. Photoelectric heating by far-UV radiation impinging on dust grains only allows the highest density ($n \gtrsim 10^3\,\mathrm{cm}^{-3}$) gas to cool down to ~ 10 K. The gas in the MW-low-no-RT simulation on the other hand reaches the minimum temperature threshold even at relatively low densities of about $n \sim 1\,\mathrm{cm}^{-3}$. The effect of photoheating from ionizing radiation is also clearly visible in the MW-high run. The high-density photoheated gas around newly formed stars clusters around $\sim 2 \times 10^4$ K, driving small scale winds and thereby preprocessing the sites of SN explosions. This high-density, warm phase is non-

existent in the MW-low-no-RT run due to the lack of radiation fields.

Fig. 4 shows the distribution of gas mass (top panels) and volume (bottom panels) as a function of density of the gas in the disc ($R < 10$ kpc and $|z| < 1.5$ kpc) at 1 Gyr. Each distribution is further divided into the contribution from molecular (purple dashed curve; $T < 100$ K), cold neutral (CNM; blue dashed curve; $100 \leq T < 1000$ K), warm neutral (WNM; green dashed curve; $1000 \leq T < 8000$ K), warm ionized (WIM; yellow dashed curve; $8000 \leq T < 10^5$ K) and hot (red dashed curve; $T \geq 10^5$ K) phases of the gas.[1] The vertical dashed line denotes the star formation density threshold of $n = 10^3\,\mathrm{cm}^{-3}$. The overall mass and volume distribution is quite similar in both the MW-high (left-hand panels) and the MW-low-no-RT (right-hand panels). The distribution of the various temperature phases (especially the colder phases ($T \lesssim 8000$ K) on the other hand is quite different. Without radiation, almost all the gas above $n \gtrsim 100\,\mathrm{cm}^{-3}$ is in the molecular phase but photo- and photoelectric heating increases the presence of the cold and warm neutral phases in the dense gas. Photoheating also creates H II regions around newly formed young stars increasing the amount of dense and warm ionized gas in the ISM. Quantitatively, the amount of molecular, cold neutral, warm neutral, warm ionized, and hot gas changes from 1 per cent, 13 per cent, 25 per cent, 58 per cent, and 3 per cent in the run with radiation fields to 4 per cent, 41 per cent, 22 per cent, 31 per cent, and 2 per cent in the run without them.

We note that in the absence of radiation fields most of the gas phases follow a lognormal density distribution that overlap with each other. However, the molecular, CNM, WNM, and WIM in the fiducial run deviates from the lognormal distribution above the star formation density threshold, with the warm gas fraction increasing at these high densities. This is due to photoheating of gas by newly formed stars. The change in the volume distribution is less noticeable because the warm ionized and the hot gas dominates the volume distribution of the ISM in both the runs. It is therefore, quite clear that local radiation from stars plays an important role in governing the phase-space structure of the the ISM, mainly via photo- and photoelectric heating.

3.2 Distribution of molecular hydrogen

We now turn our attention to the distribution of molecular hydrogen as predicted by the non-equilibrium chemical network. The typical H_2 fractions are set primarily by competition between dust-phase formation (sensitive to the local dust-to-gas ratio) and destruction by LW radiation which is sensitive to the local radiation field. Fig. 5 shows face-on (top panels) and edge-on (bottom panels) maps of atomic (left-hand panels) and molecular molecular (right-hand panels) hydrogen fractions in the MW-high simulation at 1 Gyr. The H I distribution extends to about 15 kpc from the centre of the disc, while the H_2 is only found within the central ~ 10 kpc. Molecular gas is also more clumpy and found in the highest density regions of the disc. The higher gas pressure in the disc mid-plane allows for a greater prevalence of H_2 , which can clearly be seen in the edge-on view of the disc.

---

[1]We note that these classifications are all based on the temperature of the gas alone and do not reflect its ionization state. However, almost all the cold and warm neutral gas is neutral and the warm ionized gas is mostly ionized. There is some cross-contamination, but it is minimal because most of the photoionized gas gets heated to the warm ionized phase.
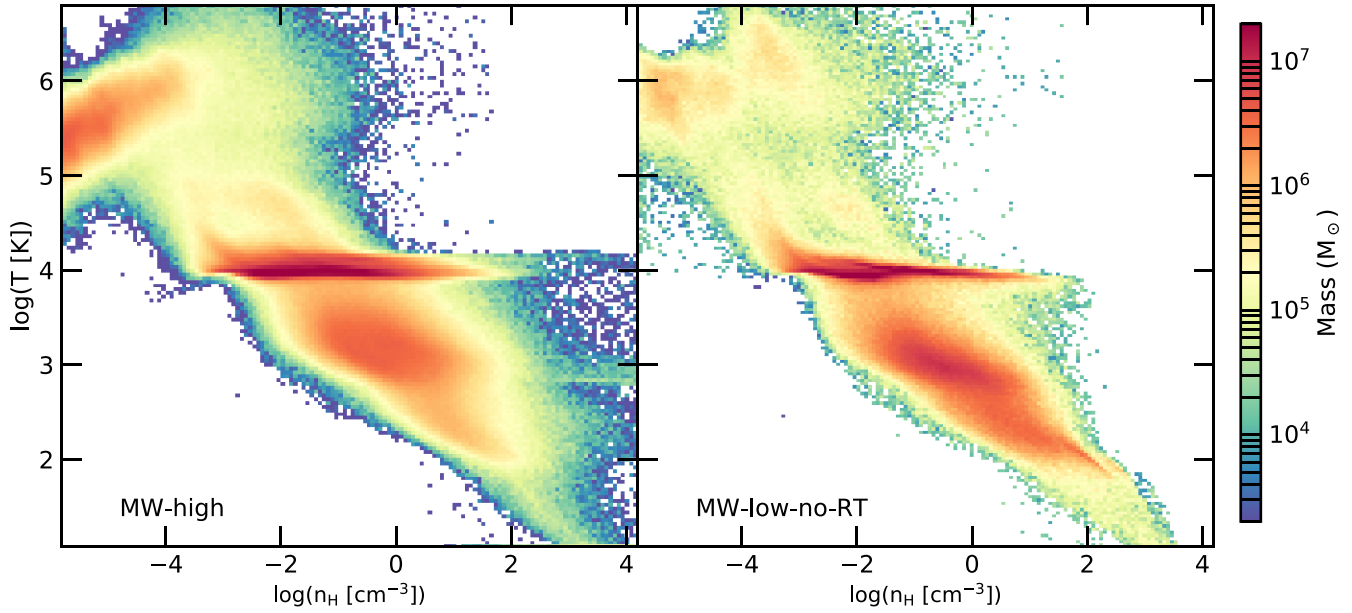
Figure 3. The temperature–density phase space diagram of all gas, colour coded by the gas mass in the MW-high (left-hand panel) and MW-low-no-RT (right-hand panel) simulations.
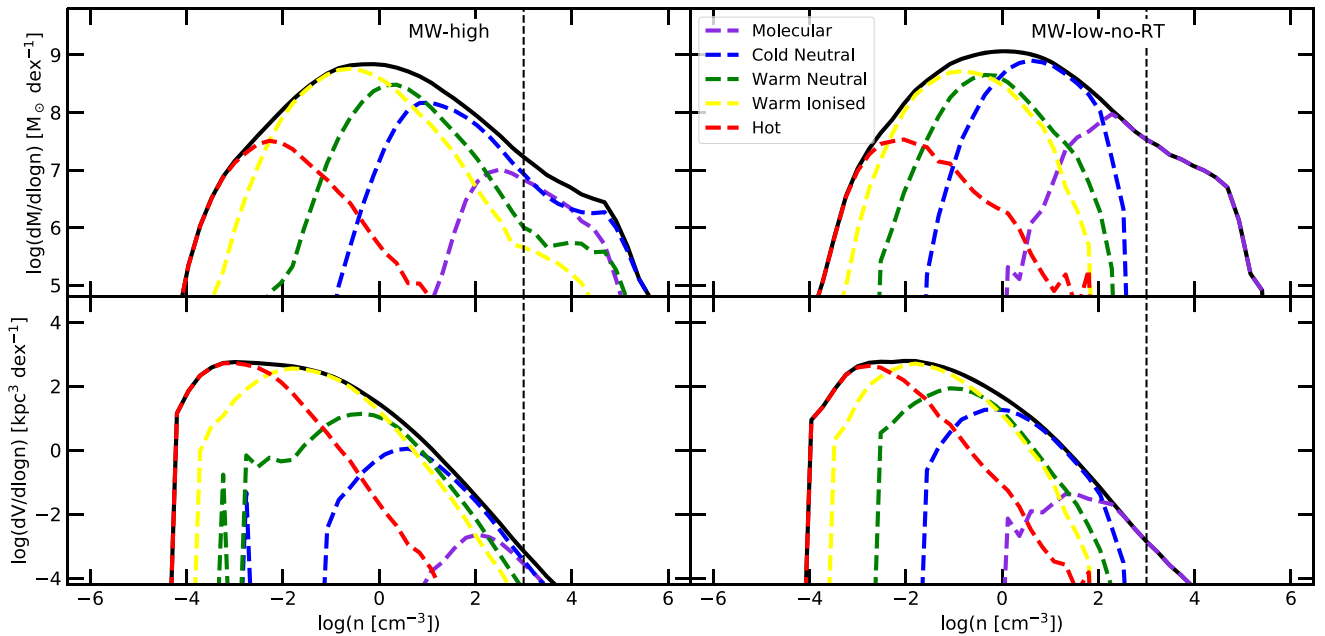

Figure 4. The mass (top panels) and volume (bottom panels) distribution of gas in the disc ($R < 10$ kpc and $|z| < 1.5$ kpc) in the MW-high (left-hand panels) and MW-low-no-old (right-hand panels) simulations. The black curve shows the distribution for all the gas in the disc, while the purple, blue, green, yellow, and red curves denote the mass and volume distribution of the molecular ($T < 100$ K), cold neutral ($100 \leq T < 1000$ K), warm neutral ($1000 \leq T < 8000$ K), warm ionized ($8000 \leq T < 10^5$ K), and hot ($T \geq 10^5$ K) gas, respectively.

A more quantitative picture can be obtained by studying the correlation between the sites of star formation and the distribution of H$_2$. It has been well known for some time that these quantities correlate with each other on sub-kpc scales (Bigiel et al. 2008; Leroy et al. 2008). Fig. 6 shows the molecular Kennicutt–Schmidt relation (Schmidt 1959; Kennicutt 1989), derived from the MW-high simulation (red points) at 1 Gyr. For comparison, the observational estimates from Leroy et al. (2008) are shown by black crosses, with the solid black line denoting the mean relation. In order to make

an accurate comparison with the observational data, we create a map of the star formation rate surface density (stars formed less $\sim$50 Myr ago). We then pick out the peaks of this distribution[2] and compute the star formation rate and H$_2$ mass within a circle of radius 750 pc around the peaks. The simulations do a very

---

[2]We use ASTRODENDRO, a Python package to compute dendrograms of Astronomical data (http://www.dendrograms.org).
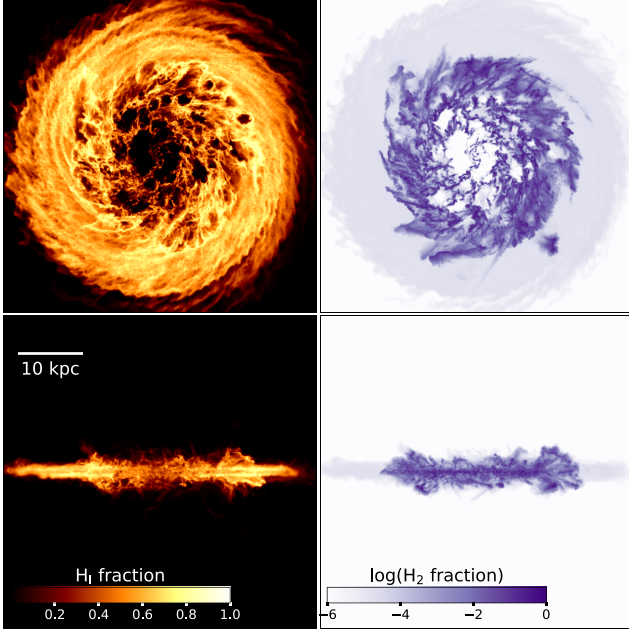
Figure 5. Face-on (top panels) and edge-on (bottom panels) maps of atomic (H I, left-hand panels) and molecular (H₂, right-hand panels) hydrogen fraction in the MW-high simulation.
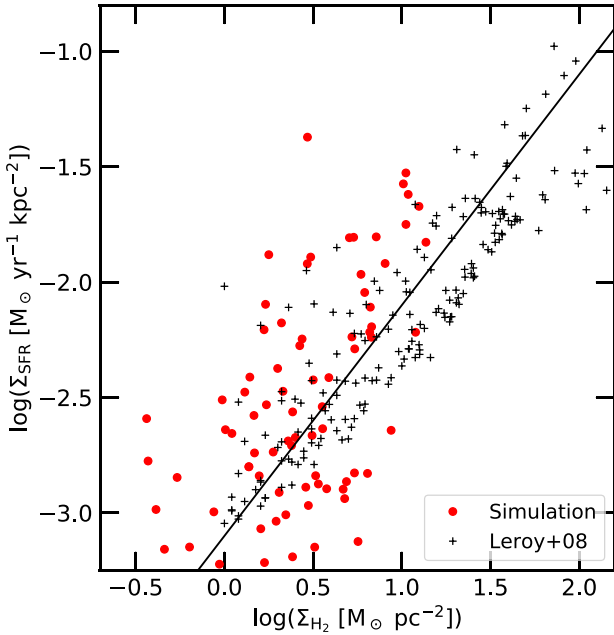

Figure 6. The molecular KS relation (red points) compared to the observational estimates (black crosses and line) taken from Leroy et al. (2008).

good job of matching both the scatter and the mean observational relation.

We note that the simulation overshoots the observed relation at very high star formation rate surface densities ($\sim 0.03 \, M_\odot \, \mathrm{yr}^{-1} \, \mathrm{kpc}^{-2}$), corresponding to gas depletion times (τ_dep) of ~ 0.5 Gyr, compared to $\tau_\mathrm{dep} \sim 2$ Gyr in the other regions of the galaxy. This point lies in the centre of the disc where the gravitational potential is the highest. This attracts gas to the centre, inducing a central starburst. These newly formed stars explode as SNe and

clears out the gas from the centre. This reduces the gas density and therefore pushes the current depletion times to less than a Gyr. We note that other works who have tried to self-consistently model H₂ have faced similar issues (Gnedin, Tassis & Kravtsov 2009). Introducing a varying clumping factor to account for unresolved dense cores in GMCs (Lupi et al. 2018), seems to alleviate this problem. In order to keep our model as simple as possible, we chose not to introduce this extra free parameter in the simulations.

Finally, we show in Fig. 7 the cumulative mass distribution of H₂ as a function of density (left-hand panel), temperature (middle panel), and H₂ fraction (right-hand panel) of the gas in the MW-high (red curves), MW-low (blue curves), MW-low-no-old (orange curves), and MW-low-no-RT (green curves) simulations. Without any radiation fields, H₂ begins to form at densities of $n_\mathrm{H} \sim 10^{-2} \, \mathrm{cm}^{-3}$, which is the self-shielding density to UVB, while the runs with RT delay the formation for H₂ to slightly higher values. The higher the radiation intensity, the larger the density of the gas needs to be in order to self-shield, shifting the H₂ mass distribution. The temperature distribution is quite intriguing, with the runs with radiation fields shifting the H₂ mass distributions to higher temperatures. This can be explained by the fact that stars are generally formed in the high-density gas implying that the radiation field strengths are higher in this part of the phase space. The high-energy H₂ and H I ionizing photons heat up the gas to temperatures of $\sim 10^4$ K, but they also have the highest interaction cross-sections, implying that they are attenuated close to the source. The far-UV photons, on the other hand, have larger mean free paths as they are attenuated only by dust grains, allowing them to penetrate the self-shielded high-density cold gas. They heat up the gas through photoelectric heating (without affecting the ionization state of the gas), shifting the H₂ mass distribution to higher temperatures. Finally, the H₂ distribution is quite similar in all the runs with respect to the ionization fraction of the gas.

3.3 Dust distribution in the ISM

We now consider the properties of the dust distribution in the ISM. Fig. 8 shows face-on (top panels) and edge-on (bottom panels) maps of the dust-to-gas ratio (D; left-hand panels) and the dust temperature (T_d, right-hand panels) in the MW-high simulation at 1 Gyr. The dust-to-gas ratio hovers around a value of $\gtrsim 0.01$ over the entire inner star forming disc (≤ 10 kpc). The outer low density, warm H I disc ($n_\mathrm{H} \sim 1 \, \mathrm{cm}^{-3}$; $T \sim 10^4$ K) is devoid of dust, because there is no star formation activity in this region. Interestingly, dust is also present outside the disc, in the CGM of the galaxy. This dust has formed in the disc and was blown out by stellar feedback-driven outflows. A similar trend is also found in the dust temperature maps. The radiation fields from stars from the inner disc heats up the dust to about ~ 20 K on average. The central star forming region shows much higher dust temperatures of ~ 30–40 K. The edge-on view shows that the temperature of extraplanar dust is higher, perpendicular to the disc and colder along it. This is because the radiation from stars preferentially escapes along the angular momentum axis of the disc, due to the lower optical depth in this direction.

Fig. 9 shows the dust mass-weighted radial profile of D relative to the canonical Milky-Way value ($D_\mathrm{MW} = 0.01$) in the MW-high (red curve) and MW-low (blue curve) simulations at 1 Gyr. Both simulations show an increase in D towards the centre of the galaxy, where the star formation rate is higher, reaching values of up to $D \sim 0.01$. The ratio slightly decreases as we get to larger galactocentric radius to a value of about ~ 0.009 at a distance of 25 kpc. The radial dependence of D in our simulations is shallower than what is observed in the MW (Giannetti et al. 2017). This is due to the fact that we do not
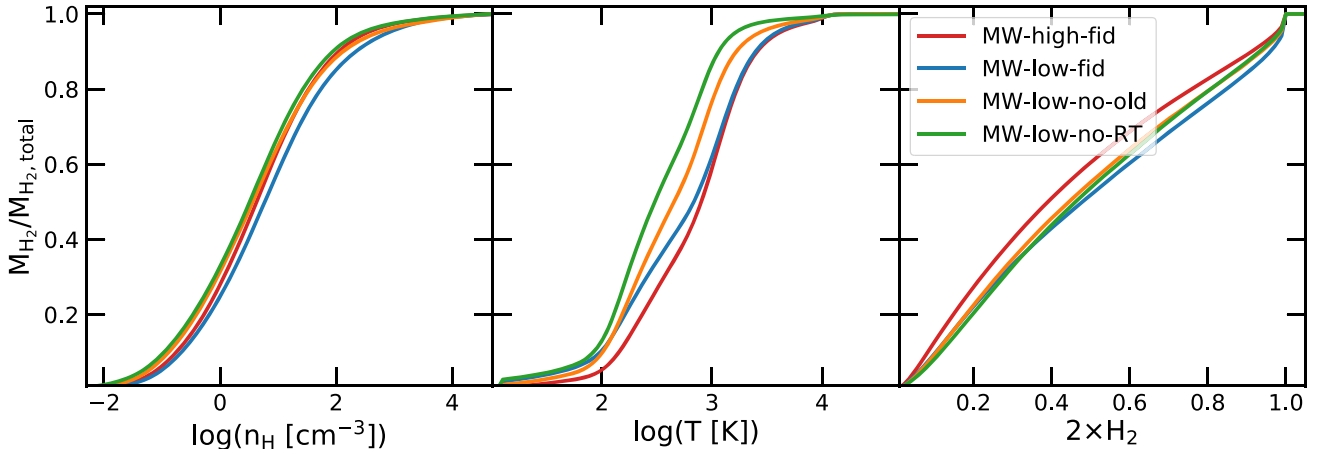
Figure 7. Cumulative mass distribution of H₂ as a function of density (left-hand panel), temperature (middle panel), and H₂ fraction (right-hand panel) of the gas in the MW-high (red curves), MW-low (blue curves), MW-low-no-old (orange curves), and MW-low-no-RT (green curves) simulations.
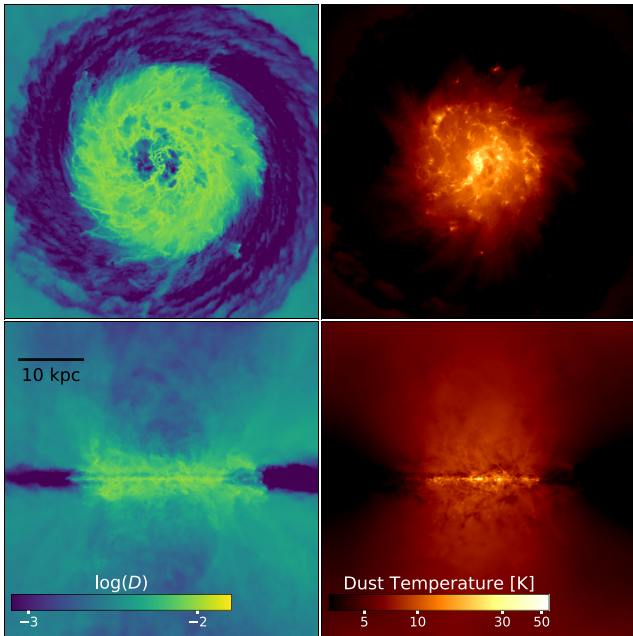

Figure 8. Face-on (top panels) and edge-on (bottom panels) maps of the dust-to-gas ratio (left-hand panels) and dust temperatures (right-hand panels) in the MW-high simulation.
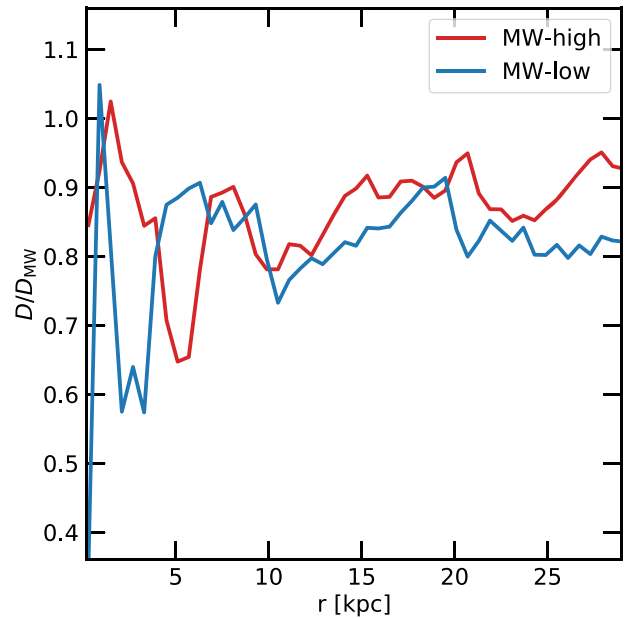

Figure 9. Dust-to-gas ratio relative to the canonical MW value (0.01) as a function of radial distance in the MW-high (red curve) and MW-low (blue curve) simulations.

have pristine circumgalactic gas around the disc, which would cool and mix with the gas in the disc, diluting its metallicity. The various resolutions give slightly different results, with the low resolution run showing a larger radial dependence than the MW-high simulation. This indicates that the dust produced in the central star forming region is more efficiently transported outwards in the high resolution simulation compared to the low resolution run.

Fig. 10 plots D/D_{MW} as a function of the gas density (left-hand panel), gas temperature (middle panel), and the ionization state of the gas (right-hand panel) in the low and high resolution fiducial simulations. The solid lines show the median relations and the dashed lines show the 10 and 90 percentile of the distribution in the high resolution run. The results are taken after 1 Gyr of simulation time and considers only gas present in the disc, which is defined by $R < 10\,\mathrm{kpc}$ and $-1.5 < z(\mathrm{kpc}) < 1.5$. D is a strong function of the

density of the gas, with the highest density gas, $n_H \gtrsim 10^4\,\mathrm{cm}^{-3}$, having a median dust-to-gas ratio of about $D \sim 0.012$. The value decreases as the density of the gas decreases with $D \lesssim 2 \times 10^{-3}$ at $n_H \lesssim 10^{-4}\,\mathrm{cm}^{-3}$. The dust distribution shows a very interesting dependence on the temperature of the gas. Below $T \lesssim 10^4\,\mathrm{K}$, D is constant with a value of ~ 0.012. There is a precipitous drop by almost a factor of two ($D \sim 6 \times 10^{-3}$) at $10^4\,\mathrm{K}$. It is noteworthy that this transition happens at roughly the photoheating temperature of soft spectral sources like high mass stars and is also close to the collisional ionization temperature of atomic hydrogen at the typical densities in the ISM. In essence, this is the temperature at which the ISM transitions from a largely neutral state to an ionized one. This clearly indicates that the dust abundance correlates with the ionization state of the gas, which is shown explicitly in the right-hand panel of Fig. 10. D reduces from ~ 0.011 in neutral gas to
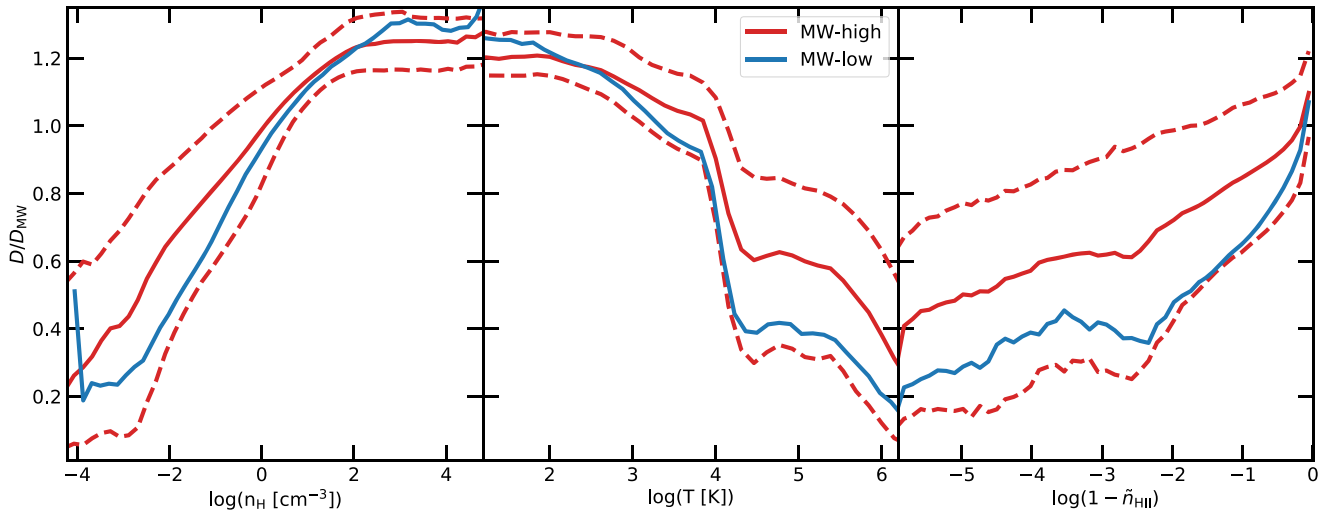
Figure 10. Dust-to-gas ratio relative to the canonical MW value as a function of density (left-hand panel), temperature (middle panel), and ionization state (right-hand panel) of the gas in the MW-high (red curves) and MW-low (blue curves) simulations.

$\sim 3 \times 10^{-3}$ in the highly ionized medium. The only processes capable of heating the gas to these temperatures are photoheating and SN explosions, which are spatially correlated. The destruction of dust in SN shocks (as given by equation 16) and dust sputtering at high temperatures (equation 17) reduce the dust content around sites of star formation. We note that dust destruction seems to be slightly more effective in the low resolution runs compared to the high resolution one, as evidenced by the higher D in the high temperature, high ionization gas in the MW-high simulation. We note that the scatter in these relations is quite high with a value of about 0.002 in the neutral, high density low temperature gas and increasing to about 0.006 in the hot low density medium. These plots clearly show that D is not constant, as has been assumed in many previous simulation works (e.g. Rosdahl & Teyssier 2015; Costa et al. 2018).

We now turn our attention to the resolved scaling relations of dust with respect to the stellar and gas mass of the galaxy. Fig. 11 shows the ratio of the dust to stellar mass (left-hand panel) as a function of the stellar surface density for the MW-high simulation (red open circles) at 1 Gyr. This plot is generated by dividing the inner disc ($R < 10$ kpc) into 1 kpc^2 areas and we calculate the quantities for each portion. The thin black line shows the median of the results from our simulation. We compare our results to the observational estimates taken from the *Herschel* Reference Survey (HRS; Boselli et al. 2010; Cortese et al. 2012) and The *Herschel* Exploitation of Local Galaxy Andromeda project (HELGA; Fritz et al. 2012; Viaene et al. 2014). The HRS sample consists of ~ 300 nearby galaxies and is sensitive to the cold dust component. The HELGA project focuses on the characteristics of the extended dust emission of Andromeda at a high spatial resolution (~ 0.6 kpc). These data sets therefore cover both the galaxy integrated and resolved properties of dust in the nearby Universe. The simulations show that the dust-to-stellar mass ratio decreases with increasing stellar surface density and is in rough agreement with both the HELGA (dashed green curve) and the H I-normal (brown curve) and H I-deficient (purple curve) HRS observational samples, although the median relation is slightly lower than what is observed.

The right-hand panel of Fig. 11 plots the ratio of the dust to atomic hydrogen mass as a function of the stellar mass surface density. This

ratio is roughly constant at a value of about $\sim 10^{-1.55}$ (red solid curve), irrespective of the stellar surface density. This is a bit higher than the average value for H I-normal systems ($\sim 10^{-2.1}$) but has remarkable agreement with the results for H I- deficient galaxies ($\sim 10^{-1.50}$) in the HRS sample (Cortese et al. 2012). The scatter in the relation is also quite similar to the observational estimates. We note that our results are more in agreement with the H I-deficient galaxies, because, the lack of pristine gas inflow from the CGM in our simulation makes the gas in the centre more dust enriched than usual, mimicking the properties of galaxies that are deficient in atomic hydrogen. These two plots together show that the dust-to-stellar mass ratio decreases due to a corresponding decrease in the gas fractions with increasing stellar surface density, which has been shown to be true observationally (Catinella et al. 2010; Cortese et al. 2011).

3.4 Dust temperature distribution

This section examines the dust temperatures (T_d) predicted by our simulations. Dust temperature depends on the composition and sizes of the dust grains, and on the interstellar radiation field (ISRF). Most of the far-UV and visible light from stars is absorbed by dust and reradiated in the IR regime. It is well known that the dust in galaxies is in radiative equilibrium with the ISRF (Draine 2003). At high redshifts, various works have inferred the dust mass and temperatures from the integrated SEDs of unresolved objects (Scoville et al. 2014; Genzel et al. 2015). Resolved studies of dust properties are possible for the local group galaxies like the LMC, the SMC, (e.g. Meixner et al. 2013; Chastenet et al. 2017), M31 (e.g. Fritz et al. 2012; Draine et al. 2014), and M33 (Braine et al. 2010; Xilouris et al. 2012). Since we assume that the dust size distribution is fixed, the dust temperatures are set mainly by radiative equilibrium between the infrared radiation field and the dust.

In Fig. 12 we show the normalized histogram of dust mass as a function of dust temperature (left-hand panel) compared to observational estimates inferred from the *Herschel* telescope for the LMC (black circle), the SMC (black diamond), M31 (inverted triangle), and M33 (black pentagon) (Utomo et al. 2019). In order
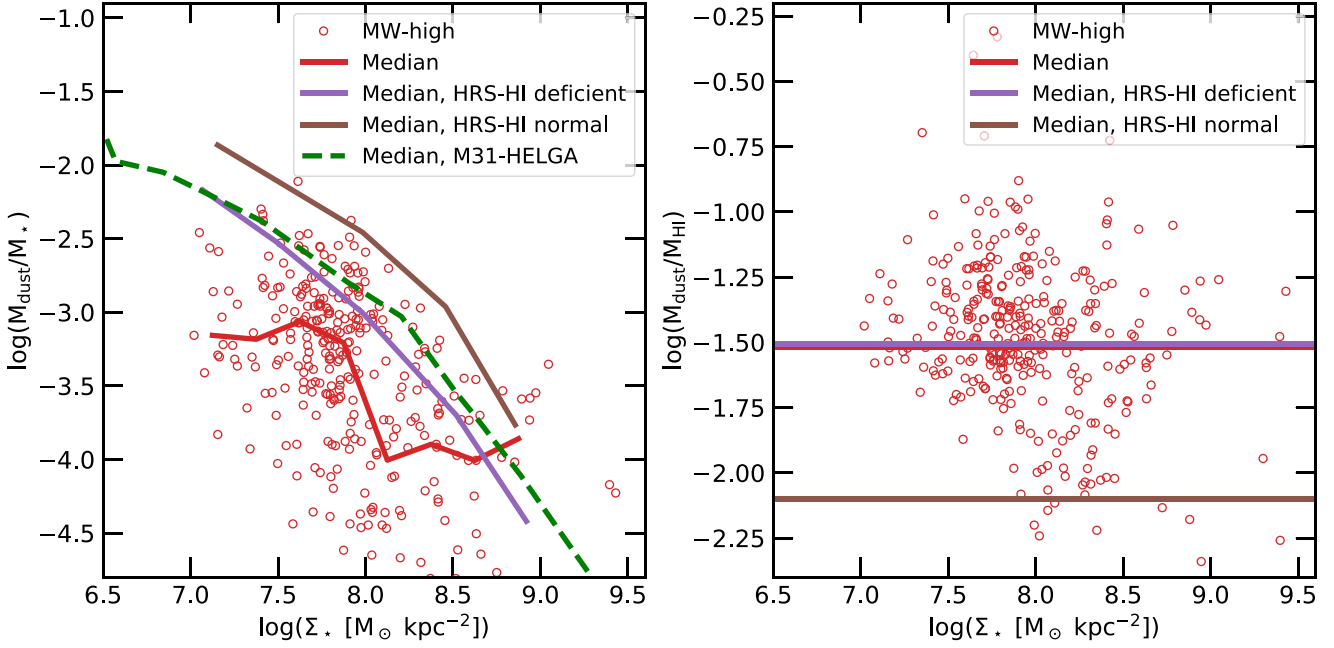
Figure 11. Ratio of the dust to stellar mass (left-hand panel) as a function of the stellar surface density. The red open circles show the results from the MW-high simulation. The red line shows the median of the simulation results, the purple and brown curves show the median relation for the H I deficient and H I normal galaxies from the HRS sample (Cortese et al. 2012), and the dashed green line denotes the median relation for M31 taken from the HELGA sample (Viaene et al. 2014). The right-hand panel shows the ratio of the dust to atomic hydrogen mass in the galaxy as a function of stellar surface density. The simulated median value of this ratio (red solid curve) is close to the observational estimates for the H I deficient sample from HRS (purple curve).
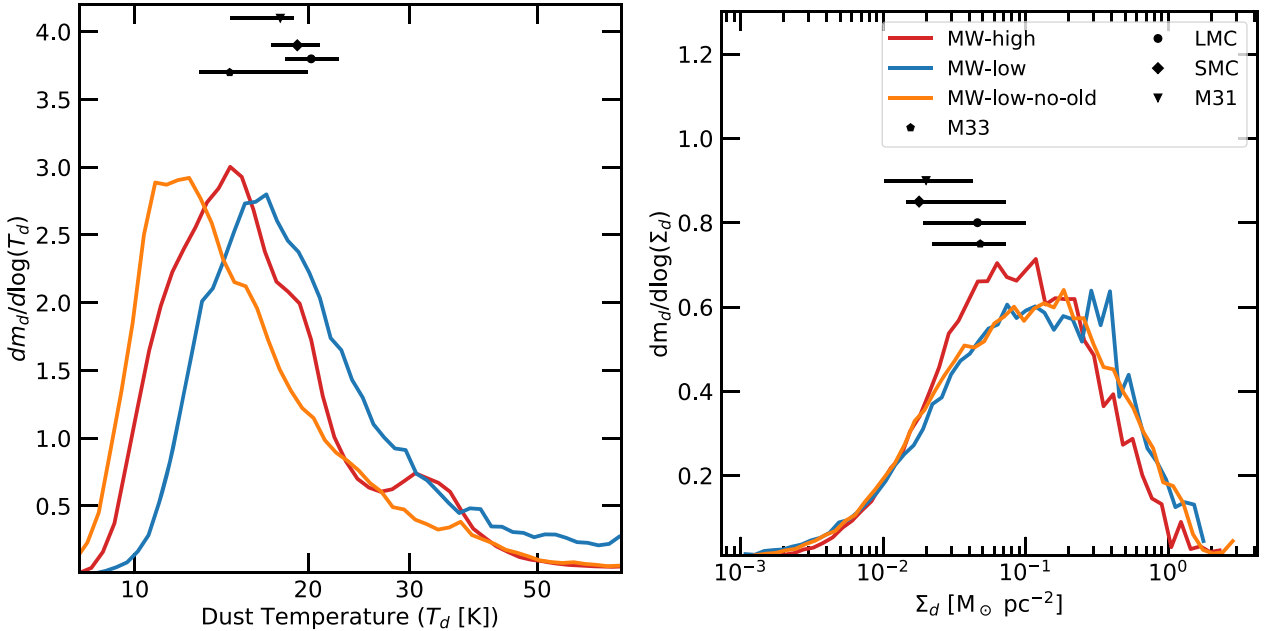

Figure 12. Normalized dust temperature (left-hand panel) and surface density (right-hand panel) distributions in the MW-high (red curve), MW-low (blue curve), and MW-low-no-old (orange curve) simulations. The black points show the observational estimates for the LMC (circle), the SMC (diamond), M33 (pentagon), and M31 (inverted triangle) taken from Utomo et al. (2019).

to be consistent with the observations, we divide the inner 10 kpc of the disc into regions, $167 \times 167\,\mathrm{pc^2}$ in size and calculate the average dust, temperature, surface density, and mass for each portion of the disc. The histogram in the MW-high (red curves) peaks at about ∼15 K, while the MW-low (blue curve) has a higher mean

dust temperature of about 18 K. This slight difference in the dust temperatures can be attributed to the fact that the high resolution run has slightly lower star formation rate (∼2 $\mathrm{M_{\odot}\,yr^{-1}}$) compared to the low resolution run (∼3 $\mathrm{M_{\odot}\,yr^{-1}}$). Both the runs show a high temperature tail extending to $T_d \gtrsim 50\,\mathrm{K}$. The dust temperatures in
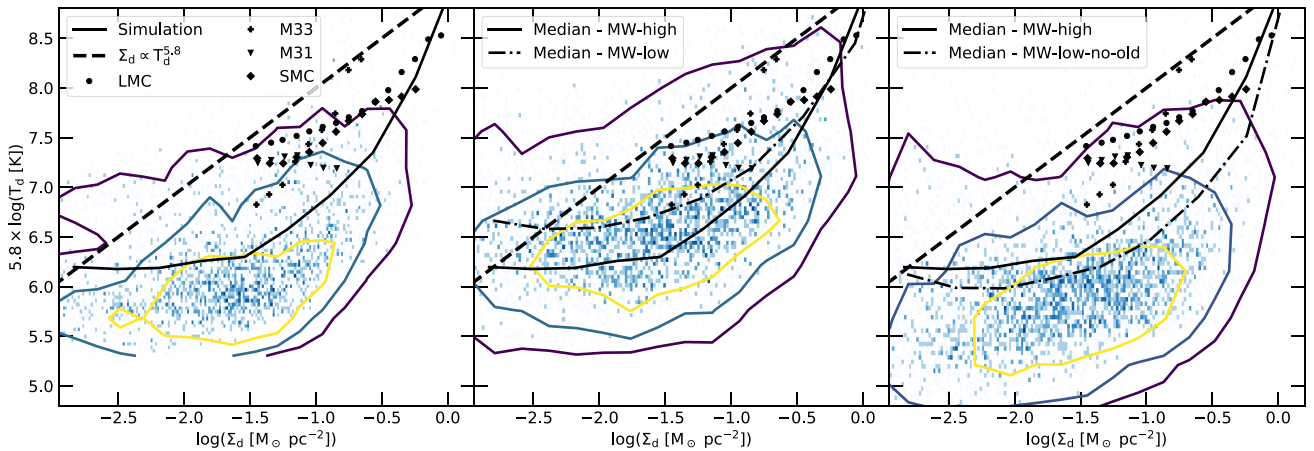
Figure 13. 2D histograms showing the dust temperature–dust surface density relation in the MW-high (left-hand panel), MW-low (middle panel), and MW-low-no-old (right-hand panel) simulations. The contours indicate the 80 per cent (purple contour), 50 per cent (blue contour), and 20 per cent (yellow contour) enclosed fractions of the distribution. The solid black line denotes the median of the distribution, and the dashed black curves indicates $\Sigma_d \propto T_d^{5.8}$, valid for dust heated by star formation. The black points show observational estimates for the LMC (circles), the SMC (diamonds), M33 (pentagons), and M31 (inverted triangles) taken from Utomo et al. (2019).

the local group galaxies range between values of 10 K and 40 K and the median lies in between 15 and 22 K, which is consistent with our simulation results (Utomo et al. 2019). In order to understand the role of old stars in dust heating, we also show results from the MW-low-no-old simulation (orange curves), which as described before, only considers radiation from stars that have formed after the start of the simulation. The fiducial models meanwhile account for radiation from both the newly formed stars and from stars that were present in the initial conditions. Not considering the radiation field from old stars only slightly reduces the dust temperatures. We do note that the high temperature wing, although still present in the MW-low-no-old simulation, is less prominent than in the fiducial runs. In the right-hand panel of Fig. 12, we show the corresponding normalized histogram of dust mass as a function of dust surface density in the simulations considered. The dust surface densities are a bit more converged, but are about a factor of ∼2 higher than what is observed in the local group galaxies. While the observed dust densities range from about $0.01\,M_\odot\,pc^{-2}$ to about $0.5\,M_\odot\,pc^{-2}$ (Utomo et al. 2019), the simulated dust densities, on the other hand, range from $0.01\,M_\odot\,pc^{-2}$ to about $1.5\,M_\odot\,pc^{-2}$. We note that there is essentially no difference between the dust surface density distributions in the three runs. Therefore, the difference in the dust temperature distributions can be attributed to the increase in the ISRF in the fiducial runs compared to the run without radiation fields from old stars.

This is seen more clearly in Fig. 13, which shows the 2D histogram of the dust temperature and dust surface densities, compared to the observational estimates. The contours indicate the 80 per cent (purple contour), 50 per cent (blue contour), and 20 per cent (yellow contour) enclosed fractions of the distribution. The solid black line denotes the median of the distribution, and the dashed black curve is the $\Sigma_d \propto T_d^{5.8}$ relation, valid for dust heated by star formation (Utomo et al. 2019). This scaling relation is obtained by assuming an empirically fitted opacity law ($\beta = 1.8$), and assumes that the dust is optically thick to its own re-emission. In general ISM conditions, these assumptions are only partially valid, explaining the typically lower dust temperatures observed in nearby galaxies. The fiducial high resolution simulation (MW-high; left-hand panel) shows a reasonable match with the observational results. The MW-
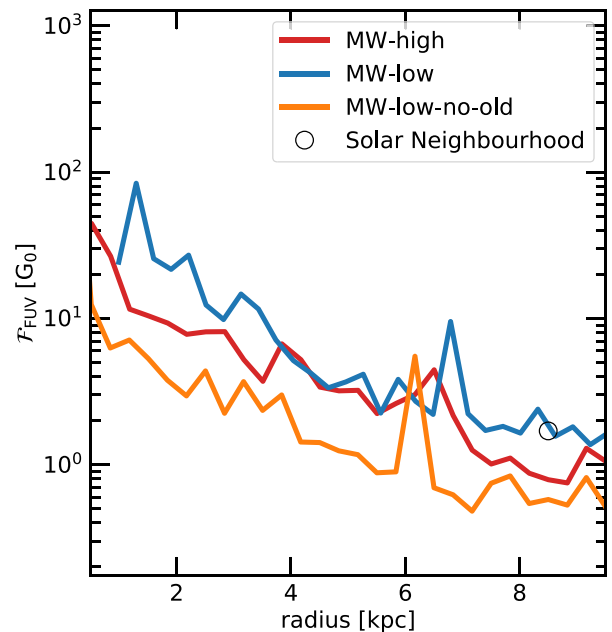

Figure 14. Value of the FUV flux (in units of G_0) as a function of radial distance for the MW-high (red curve), MW-low (blue curve) and MW-low-no-old (orange curve) simulations. The solar neighbourhood value is indicated by the black point (Habing 1968).

low simulation (middle panel) has a median dust temperature slightly higher than the high resolution simulation, which can be attributed to different star formation rates. The run without radiation fields from old stars (MW-low-no-old; right-hand panel), shows consistently lower dust temperatures despite a higher star formation rate. The difference is larger at lower surface densities implying that the contribution to dust heating from old stars is more important in low dust surface density regions. Therefore, we conclude that old stellar populations play a non-negligible role in heating up the dust in galaxies (Groves et al. 2012; Kirkpatrick et al. 2014; Leja et al. 2019).
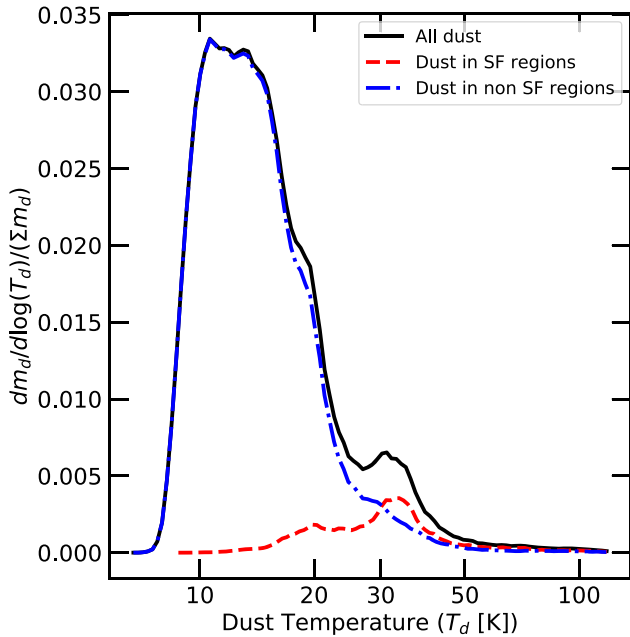
Figure 15. Temperature distribution of all the dust in the MW-high simulation (black curve), split by dust temperature in star-forming (red dashed curve) and non-star-forming regions (blue dot-dashed curve).

This difference in the dust temperatures is caused by the difference in the ISRFs in the simulations with and without radiation contribution from old stars as seen in Fig. 14, which plots the flux of the far-UV radiation field ($5.8 - 11.2$ eV) in units of the Habing value ($G_0 = 1.6 \times 10^{-3}$ erg s^{-1} cm^{-2}; Habing 1968) as a function of galactocentric distance. Both the fiducial simulations (MW-high: red curve and MW-low: blue curve) show a value of the ISRF that is higher than the MW-low-no-old (orange curve). This translates to an increase in the temperature of the dust by a factor of about ∼1.5, which explains the differences in Figs 12 and 13. We also note that the fiducial runs more closely match the solar neighbourhood value of the ISRF (black circle), while the MW-low-no-old run shows a value which is quite a bit lower.

Finally, Fig. 15 shows the mass-weighted dust temperature distribution normalized to the total dust mass (solid black curve), similar to Fig. 12, but now decomposed into dust in star-forming (dashed red curve) and non-star-forming (blues dot-dashed curve) regions. Star-forming regions are taken to be any dust present within 1 kpc of the sites of star formation. These sites are determined by creating a map of the star formation rate surface density (stars formed less ∼50 Myr ago). The peaks of this distribution are taken as centres of the sites of star formation. As expected, the star-forming regions tend to have warmer dust temperatures of about ∼35 K, due to the higher radiation field strengths, while the old stellar population heats the rest of the dust to about ∼18 K. Since most of the disc is in non-star-forming regions, the dust temperature distribution peaks at this temperature.[3] This result is in agreement with observational estimates of dust temperature in star-forming regions in local group galaxies (Relaño & Kennicutt 2009; Tabatabaei & Berkhuijsen 2010; Utomo

---

[3]We note that the secondary peak in the dust temperature distribution at about ∼20 K in the star forming regions is because the choice of 1 kpc radius around star formation peaks is quite arbitrary, implying that the selected regions will also be polluted by dust heated by the old stellar population.

et al. 2019). This explains the cold dust temperature peak and the warm dust temperature wing seen in the dust temperature distribution in our simulations.

4 SUMMARY AND CONCLUSIONS

In this paper, we present a state-of-the-art model to self-consistently treat the effects of radiation fields, dust physics, and molecular chemistry in the interstellar medium of galaxies. This work builds on the resolved ISM model SMUGGLE, introduced in Marinacci et al. (2019). We retain the star formation, SN, and stellar wind feedback prescriptions, and the metal enrichment strategies of SMUGGLE. We replace the subgrid radiation feedback prescriptions for photoheating and radiation pressure with accurate radiation hydrodynamics. Our model also introduces more realistic prescriptions for the gas cooling and heating processes that occur in the low temperature ($\lesssim 10^4$ K) ISM by replacing CLOUDY fits to the cooling rates with a model for cooling via fine structure metal lines combined with cooling from molecular hydrogen and dust-gas collisions. Photoheating from ionizing radiation and photoelectric heating from far-UV radiation impinging on dust grains are calculated from the radiation fields generated from the stars in the galaxy. Moreover, as the abundance of molecular hydrogen and dust are important for determining the cooling and heating rates of gas in the ISM, we endeavour to model them in a self-consistent manner. The abundance of molecular hydrogen is estimated using a non-equilibrium thermochemical network. The ionization and heating rates are set by the local radiation field strength of each cell. Dust is modelled using the method outlined in McKinnon et al. (2016), which accounts for dust production in SN and AGB stars, dust destruction via SN events, and thermal sputtering in the high temperature gas. In addition, we introduce a scheme to estimate the dust temperature distribution. The dust abundances and temperatures in turn control the formation rate of H$_2$ and the cooling rate via dust-gas collisions.

We tested this model in simulations of an isolated non-cosmological Milky Way-like disc. Our main findings are:

(i) After an initial starburst phase, the star formation rates are maintained at a value of about ∼2–3 M$_\odot$ yr^{-1} throughout the entire simulation time, consistent with observational data. There is no real difference in the star formation rates in the runs with and without radiation feedback. This confirms findings from previous works that in low gas surface density environments the effect of radiation feedback is modest in regulating kpc scale averaged star formation rates.

(ii) Radiation from stars drastically changes the phase structure of the interstellar medium via photoheating and photoelectric heating. These heating mechanisms reduce the amount of cold gas in the disc and at the same time increase the mass in the warm phases. The hot, SNe heated, phase remains relatively unaffected by radiation as this phase arises mainly due to SN explosions.

(iii) The H$_2$ chemistry module does a good job of reproducing the molecular, atomic, and ionized phases of the gas. Molecular hydrogen is present mainly in the high-density ($1 \lesssim n_H$ [cm^{-3}] $\lesssim 10^4$) intermediate temperature gas ($100 \lesssim$ T [K] $\lesssim 10^4$), in agreement with previous works, which allows us to largely match the Kennicutt–Schmidt relation.

(iv) The dust abundances predicted by our simulations match the values inferred for local group galaxies. We show that the dust-to-gas ratio is a complex function of gas density, temperature, and ionization state. Our dust model is also able to match the scaling relations of dust masses with stellar mass and the atomic gas present in the galaxy.

(v) The simulations reproduce observational estimates of the dust temperature distribution of local group galaxies. We also show that the median interstellar radiation field heats the dust to temperatures of about 15–20 K. The warm dust ($\sim$35 K), on the other hand, lies close to star forming regions and is heated by the action of newly formed O and B stars.

We have shown that our simulations are capable of reproducing and predicting a wide range of observables. We plan to use this state-of-the-art model to perform next-generation cosmological galaxy formation simulations that will be able to predict the resolved ($\sim$10 pc) properties of galaxies and their outflows with greater fidelity than has been possible previously. This is an important and necessary step in order to interpret observational data from current and future facilities like *ALMA*, *JWST*, *TMT*, *GMT* , and *E-ELT*, which will provide resolved imaging and spectroscopic data of galaxies all the way up to $z \sim 2$.

ACKNOWLEDGEMENTS

DATA AVAILABILITY

Raw data were generated by performing simulations at the NASA Pleiades computer. Derived data supporting the findings of this study are available from the corresponding author RK on request.

REFERENCES

Asplund M., Grevesse N., Sauval A. J., Scott P., 2009, ARA&A, 47, 481
Barnes J., Hut P., 1986, Nature, 324, 446
Benson A. J., 2010, Phys. Rep., 495, 33
Bialy S., Sternberg A., 2019, ApJ, 881, 160
Bigiel F., Leroy A., Walter F., Brinks E., de Blok W. J. G., Madore B., Thornley M. D., 2008, AJ, 136, 2846
Boselli A. et al., 2010, PASP, 122, 261
Braine J. et al., 2010, A&A, 518, L69
Bruzual G., Charlot S., 2003, MNRAS, 344, 1000
Burke J. R., Hollenbach D. J., 1983, ApJ, 265, 223
Cantalupo S., 2010, MNRAS, 403, L16
Catinella B. et al., 2010, MNRAS, 403, 683
Chastenet J., Bot C., Gordon K. D., Bocchio M., Roman-Duval J., Jones A. P., Ysard N., 2017, A&A, 601, A55
Clements D. L., Sutherland W. J., Saunders W., Efstathiou G. P., McMahon R. G., Maddox S., Lawrence A., Rowan-Robinson M., 1996, MNRAS, 279, 459
Cochrane R. K. et al., 2019, MNRAS, 488, 1779
Cortese L., Catinella B., Boissier S., Boselli A., Heinis S., 2011, MNRAS, 415, 1797
Cortese L. et al., 2012, A&A, 540, A52
Costa T., Rosdahl J., Sijacki D., Haehnelt M. G., 2018, MNRAS, 473, 4197
Davé R., Thompson R., Hopkins P. F., 2016, MNRAS, 462, 3265
Davis S. W., Jiang Y.-F., Stone J. M., Murray N., 2014, ApJ, 796, 107

Draine B. T., 1978, ApJS, 36, 595
Draine B. T., 2003, ARA&A, 41, 241
Draine B. T., Bertoldi F., 1996, ApJ, 468, 269
Draine B. T., Salpeter E. E., 1979, ApJ, 231, 77
Draine B. T. et al., 2014, ApJ, 780, 172
Dwek E., 1998, ApJ, 501, 643
Faucher-Giguère C.-A., Lidz A., Zaldarriaga M., Hernquist L., 2009, ApJ, 703, 1416
Fritz J. et al., 2012, A&A, 546, A34
Fujimoto Y., Chevance M., Haydon D. T., Krumholz M. R., Kruijssen J. M. D., 2019, MNRAS, 487, 1717
Geen S., Rosdahl J., Blaizot J., Devriendt J., Slyz A., 2015, MNRAS, 448, 3248
Genzel R. et al., 2015, ApJ, 800, 20
Giannetti A. et al., 2017, A&A, 606, L12
Glover S. C. O., Mac Low M.-M., 2007, ApJS, 169, 239
Gnedin N. Y., Abel T., 2001, New Astron., 6, 437
Gnedin N. Y., Kravtsov A. V., 2011, ApJ, 728, 88
Gnedin N. Y., Tassis K., Kravtsov A. V., 2009, ApJ, 697, 55
Gould R. J., Salpeter E. E., 1963, ApJ, 138, 393
Groves B. et al., 2012, MNRAS, 426, 892
Habing H. J., 1968, Bull. Astron. Inst. Netherlands, 19, 421
Hernquist L., 1990, ApJ, 356, 359
Hernquist L., 1993, ApJS, 86, 389
Hirashita H., 1999, A&A, 344, L87
Hollenbach D., McKee C. F., 1979, ApJS, 41, 555
Hopkins P. F., Kereš D., Oñorbe J., Faucher-Giguère C.-A., Quataert E., Murray N., Bullock J. S., 2014, MNRAS, 445, 581
Hopkins P. F. et al., 2018, MNRAS, 480, 800
Hopkins P. F., Grudic M. Y., Wetzel A. R., Keres D., Gaucher-Giguere C.-A., Ma X., Murray N., Butcher N., 2020, MNRAS, 491, 3702
Hu C.-Y., Naab T., Glover S. C. O., Walch S., Clark P. C., 2017, MNRAS, 471, 2151
Hu C.-Y., Zhukovska S., Somerville R. S., Naab T., 2019, MNRAS, 487, 3252
Indriolo N., McCall B. J., 2012, ApJ, 745, 91
Kannan R., Stinson G. S., Macciò A. V., Brook C., Weinmann S. M., Wadsley J., Couchman H. M. P., 2014, MNRAS, 437, 3529
Kannan R., Vogelsberger M., Stinson G. S., Hennawi J. F., Marinacci F., Springel V., Macciò A. V., 2016, MNRAS, 458, 2516
Kannan R., Vogelsberger M., Marinacci F., McKinnon R., Pakmor R., Springel V., 2019, MNRAS, 485, 117
Kannan R., Marinacci F., Simpson C. M., Glover S. C. O., Hernquist L., 2020, MNRAS, 491, 2088
Katz N., Weinberg D. H., Hernquist L., 1996, ApJS, 105, 19
Kennicutt Robert C. J., 1989, ApJ, 344, 685
Kim J.-G., Kim W.-T., Ostriker E. C., 2019, ApJ, 883, 102
Kirkpatrick A. et al., 2014, ApJ, 789, 130
Leja J. et al., 2019, ApJ, 877, 140
Leroy A. K., Walter F., Brinks E., Bigiel F., de Blok W. J. G., Madore B., Thornley M. D., 2008, AJ, 136, 2782
Levermore C. D., 1984, J. Quant. Spec. Radiat. Transf., 31, 149
Lupi A., Bovino S., Capelo P. R., Volonteri M., Silk J., 2018, MNRAS, 474, 2884
Ma X., Hopkins P. F., Wetzel A. R., Kirby E. N., Anglés-Alcázar D., Faucher-Giguère C.-A., Kereš D., Quataert E., 2017, MNRAS, 467, 2430
Ma X. et al., 2020, MNRAS, 493, 4315
Marinacci F., Sales L. V., Vogelsberger M., Torrey P., Springel V., 2019, MNRAS, 489, 4233
McKee C., 1989, in Allamandola L. J., Tielens A. G. G. M., eds, Proc. IAU Symp. 135, Interstellar Dust. Kluwer Academic Publishers, Dordrecht, the Netherlands, p. 431
McKinnon R., Torrey P., Vogelsberger M., 2016, MNRAS, 457, 3775
McKinnon R., Torrey P., Vogelsberger M., Hayward C. C., Marinacci F., 2017, MNRAS, 468, 1505
McKinnon R., Vogelsberger M., Torrey P., Marinacci F., Kannan R., 2018, MNRAS, 478, 2851

Meixner M. et al., 2013, AJ, 146, 62

Morgan C. W., Kochanek C. S., Morgan N. D., Falco E. E., 2010, ApJ, 712, 1129

Murray N., Ménard B., Thompson T. A., 2011, ApJ, 735, 66

Naab T., Ostriker J. P., 2017, ARA&A, 55, 59

Nickerson S., Teyssier R., Rosdahl J., 2018, MNRAS, 479, 3206

Pakmor R., Springel V., Bauer A., Mocz P., Munoz D. J., Ohlmann S. T., Schaal K., Zhu C., 2016, MNRAS, 455, 1134

Relaño M., Kennicutt Robert C. J., 2009, ApJ, 699, 1125

Rosdahl J., Teyssier R., 2015, MNRAS, 449, 4380

Rosdahl J., Blaizot J., Aubert D., Stranex T., Teyssier R., 2013, MNRAS, 436, 2188

Schaye J. et al., 2015, MNRAS, 446, 521

Schmidt M., 1959, ApJ, 129, 243

Scoville N. et al., 2014, ApJ, 783, 84

Seab C. G., Shull J. M., 1983, ApJ, 275, 652

Smith M. C., Sijacki D., Shen S., 2018, MNRAS, 478, 302

Smith M. C., Sijacki D., Shen S., 2019, MNRAS, 485, 3317

Springel V., 2010, MNRAS, 401, 791

Springel V., Hernquist L., 2003, MNRAS, 339, 289

Springel V., Di Matteo T., Hernquist L., 2005, ApJ, 620, L79

Springel V. et al., 2018, MNRAS, 475, 676

Strömgren B., 1939, ApJ, 89, 526

Tabatabaei F. S., Berkhuijsen E. M., 2010, A&A, 517, A77

Thornton K., Gaudlitz M., Janka H. T., Steinmetz M., 1998, ApJ, 500, 95

Tsai J. C., Mathews W. G., 1995, ApJ, 448, 84

Utomo D., Chiang I. D., Leroy A. K., Sand strom K. M., Chastenet J., 2019, ApJ, 874, 141

van de Voort F., Schaye J., Booth C. M., Haas M. R., Dalla Vecchia C., 2011, MNRAS, 414, 2458

Viaene S. et al., 2014, A&A, 567, A71

Vogelsberger M., Sijacki D., Kereš D., Springel V., Hernquist L., 2012, MNRAS, 425, 3024

Vogelsberger M., Genel S., Sijacki D., Torrey P., Springel V., Hernquist L., 2013, MNRAS, 436, 3031

Vogelsberger M. et al., 2014, MNRAS, 444, 1518

Vogelsberger M., Marinacci F., Torrey P., Puchwein E., 2020a, Nature Review Physics, 2, 42

Vogelsberger M. et al., 2020b, MNRAS, 492, 5167

Wetzel A. R., Hopkins P. F., Kim J.-h., Faucher-Giguère C.-A., Kereš D., Quataert E., 2016, ApJ, 827, L23

Wiersma R. P. C., Schaye J., Smith B. D., 2009, MNRAS, 393, 99

Woitke P., 2006, A&A, 452, 537

Wolfire M. G., McKee C. F., Hollenbach D., Tielens A. G. G. M., 2003, ApJ, 587, 278

Xilouris E. M. et al., 2012, A&A, 543, A74

Yozin C., Bekki K., 2014, MNRAS, 443, 522

Zhu H., Slane P., Raymond J., Tian W. W., 2019, ApJ, 882, 135

Zhukovska S., 2014, A&A, 562, A76

This paper has been typeset from a TEX/LATEX file prepared by the author.